Article

Engineering aptamer-directed phosphatase recruiting chimeras: a strategy for modulating receptor function and overcoming drug resistance

Zhilan Zhou[1,2,5], Yichang Liu [3,5], Ya Wang[2], Hang Jiang[2], Tingting Chen[2], Yingdi Zhu[2], Ting Fu[2,4] & Juan Li [2] ✉

Receptor tyrosine kinases (RTKs) play a crucial role in the regulation of intracellular signal transduction, underscoring their significance as targets for drug therapy. Despite the widespread clinical use of kinase inhibitors, the increasing occurrence of off-target effects and drug resistance makes it urgent to explore alternative approaches to modulate RTKs functions. Here, we propose an approach for attenuating cell-surface receptor signaling, termed Aptamer-directed Phosphatase Recruiting Chimeras (Apt-PRCs). The Apt-PRC is composed of an aptamer to recruit phosphatases and a binder to target receptors. As a proof-of-concept, we design and construct Apt-PRCs intended for direct dephosphorylation of tyrosine residues on the receptor targets, *i.e.*, epidermal growth factor receptor and mesenchymal-epithelial transition factor, respectively. The as-developed Apt-PRCs manage to inhibit specifically and efficiently the reception and transmission of phosphorylation signals both in vitro and in vivo. Furthermore, it is discovered that the induced dephosphorylation could enhance the susceptibility to gefitinib in drug-resistant cancer cells and a xenograft mouse model, indicating the potential of Apt-PRCs to overcome drug resistance in cancer. This work offers a versatile methodology to design molecular mediators to modulate receptor phosphorylation so as to regulate the downstream signal transduction and overcome drug resistance.

Cell surface receptors, as the most functionally diverse membrane proteins, play pivotal roles in a wide array of biological processes[1,2]. Regulation of their functions is essential for understanding their biological roles. In particular, receptor tyrosine kinases (RTKs) are extensively distributed transmembrane proteins that act as receptors for extracellular signaling molecules, including growth factors and neurotrophic factors. They regulate a wide range of complex cellular processes like cell proliferation, migration and apoptosis, and has been regarded as important drug targets for cancer and immunological disorders[3]. Up to now, many monoclonal antibodies and small molecule tyrosine kinase inhibitors (TKIs) have been developed to interfere with RTKs functions. Despite of their widespread applications in clinics, adaptive and acquired resistance remain significant challenges that limit their long-term therapeutic efficacy[4]. For instance, epidermal

[1]Academy of Medical Engineering and Translational Medicine, Tianjin University, Tianjin 300072, China. [2]Hangzhou Institute of Medicine (HIM), Chinese Academy of Sciences, Hangzhou 310022, China. [3]School of Pharmacy, Nantong University, Nantong 226019, China. [4]College of Chemistry and Chemical Engineering, Hunan University, Changsha 410082, China. [5]These authors contributed equally: Zhilan Zhou, Yichang Liu. ✉e-mail: lijuan@him.cas.cn

growth factor receptor (EGFR) small molecule TKIs, such as gefitinib, erlotinib and afatinib, have been demonstrated effective as the initial treatment for advanced non-small-cell lung cancer (NSCLC) by targeting intracellular tyrosine kinase domains[5]. However, approximately 50%-60% of patients would turn resistant against those TKIs after 8–12 months of treatment, with the development of mutations on EGFR like the T790M mutation[6]. Alternatively, monoclonal antibodies have been utilized to target the extracellular domain of EGFR receptors. Nonetheless, resistance against the antibody-therapy could also happen through activating mutations in the extracellular ligand-binding domain of EGFR[7]. The growing emergence of host resistance makes an urgent requirement for novel approaches to regulate RTKs functions.

Although anti-RTK antibodies could block ligand binding, they fail to inhibit the sustained downstream intracellular signaling pathways, which continue to activate signaling cascade and contribute to the development of resistance against the target therapy[8]. As phosphorylation is a fundamental requirement for RTKs activation[9], dephosphorylation of RTKs by phosphatases might be able to terminate their extracellular signaling initiated by growth factors and hormones. This could be achieved through activating or recruiting of cellular phosphatases. Since many phosphatases concurrently regulate multiple signaling pathways, the broad activation of a specific phosphatase may result in extensive dephosphorylation of substrates, potentially leading to unfavorable consequences in various signaling pathways[10].

In recent years, heterobifunctional molecules have garnered significant attention, with proteolysis targeting chimeras (PROTACs) standing out as a prominent example. PROTACs function by recruiting E3 ubiquitin ligases to facilitate the degradation of target proteins (POIs), achieving remarkable success. Building on the concept of PROTACs, emerging heterobifunctional molecules have been developed to selectively modulate the phosphorylation of POIs through proximity-driven mechanisms. Phosphorylation-inducing chimeric small molecules facilitate kinase-mediated phosphorylation of POIs. Phosphatase recruiting chimeras (PhoRCs) enable protein phosphatases to dephosphorylate POIs in a highly target-specific manner. Bispecific antibodies and bifunctional small molecules-based PhoRCs have been reported to accelerate dephosphorylation[11–13]. Fernandes et al. engineered a bispecific antibody-based PhoRCs, termed receptor inhibition by phosphatase recruitment (RIPR), to induce the cross-linking of the target protein PD-1 to the phosphatase CD45, thereby attenuating cell-surface receptor signaling[11]. Zhang et al. designed a bifunctional small molecular-based PhoRCs, termed DDO3711, to effectively accelerate the dephosphorylation of intracellular signaling protein ASK1 in a phosphatase PP5-recruiting manner[13]. Through altering the phosphorylation status of a specific receptor protein only while keeping its expression level unchanged, PhoRCs provide a promising approach to modulate receptor function. However, the design and production of bispecific antibodies have traditionally relied on protein engineering, which still holds some inherent drawbacks, such as laboriousness, high cost and complicated manufacture. The application of small molecule chimeras, on the other hand, is often limited by their low affinity to phosphatases, with a dissociation constant (Kd) in the micromolar range[13]. Furthermore, most small molecule chimeras are designed to target intracellular proteins rather than receptors on the cell membrane. The development of novel intervention molecules to selectively and efficiently modulate membrane receptor function thereby remains a highly desirable objective in drug design and discovery.

Aptamers have emerged as a promising tool to modulate receptor function in living cells, taking advantage of their high specificity and affinity (with Kd spanning from the picomolar to micromolar range). Moreover, the nucleic acid nature of aptamers makes their synthesis easy and cost-effective, and provides remarkable versatility to design
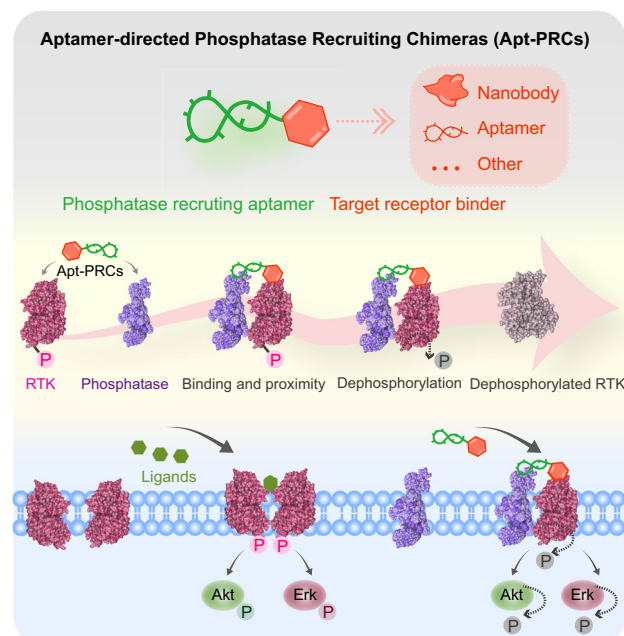

Fig. 1 | Schematic illustration of the construction and function of Apt-PRCs. The Apt-PRC is composed of an aptamer to recruit phosphatases (colored green) and a binder to target receptors (colored orange). Apt-PRCs recruit phosphatases (e.g., PTPRF) within close proximity to the target RTKs (e.g., Met, EGFR), which make the RTKs dephosphorylated and thereby modulate the RTKs functions, especially attenuating downstream Akt and Erk signaling pathways related with tumor growth.

heterobifunctional aptamer-based structures for the regulation of different receptors[14].

Herein, we develop a type of intervention molecule, called Aptamer-directed Phosphatase Recruiting Chimeras (Apt-PRCs), to selectively dephosphorylate the receptor of interest both in vitro and in vivo. As illustrated in Fig. 1, the Apt-PRC is composed of an aptamer to recruit phosphatases (colored green) and a binder to target receptors (colored orange). As a member of protein tyrosine phosphatase family, protein tyrosine phosphatase receptor type F (PTPRF) plays a crucial role in signal transduction by removing phosphate groups from tyrosine residues of proteins, and controls multiple cellular processes such as proliferation, apoptosis and migration[15,16]. Through the conjugation of PTPRF-recruiting aptamer ZAJ4a and a target receptor binder (nanobody and aptamer in this case), we design and construct the Apt-PRCs to induce direct dephosphorylation of two representative RTKs, i.e., EGFR and mesenchymal-epithelial transition factor (Met), respectively. The as-developed Apt-PRCs recruit PTPRF within close proximity to the target receptors. The phosphatase domain of PTPRF can act intracellularly on the phosphorylated tyrosine residues of EGFR and Met, aiming to inhibit specifically and efficiently the reception and transmission of the phosphorylation signals both in vitro and in vivo. Furthermore, we discover that the induced dephosphorylation could enhance the susceptibility to gefitinib in drug-resistant cancer cells and a xenograft mouse model, indicating the potential of Apt-PRCs to overcome drug resistance in cancer. In summary, this study demonstrates the application of aptamers as phosphatase recruiting molecules to induce dephosphorylation of cell surface receptors, thereby modulating the receptor function and offering a potential solution to the long-standing challenge of drug resistance in cancer therapy.

Results
Construction and characterization of Apt-PRCs
In the proof-of-concept study, we designed and constructed Apt-PRCs to recruit phosphatase PTPRF and introduce the dephosphorylation of
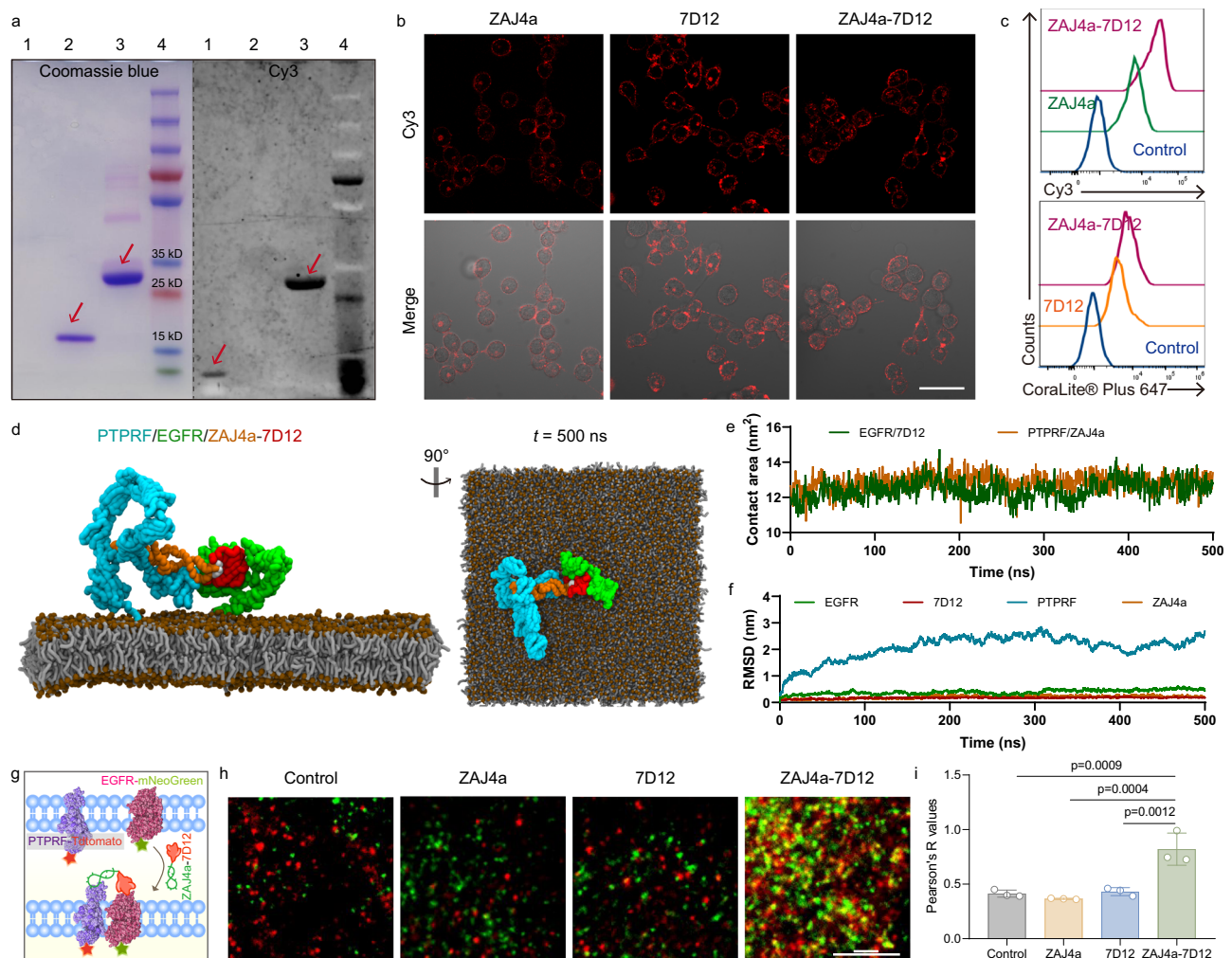
Fig. 2 | Construction and characterization of Apt-PRCs ZAJ4a-7D12. a PAGE analysis of the constructed Apt-PRCs ZAJ4a-7D12. Lane 1, ZAJ4a-Cy3; lane 2, 7D12; lane 3, ZAJ4a-Cy3-7D12; lane 4, protein makers. Cy3 was conjugated at the 5' end of ZAJ4a. Left, Coomassie bright blue staining; right, fluorescence imaging in Cy3 channel. The red arrow pointed to the target band. Uncropped gels were provided in Source Data. **b** The binding ability analysis of ZAJ4a, 7D12 and ZAJ4a-7D12 towards SACC-83 cells by CLSM in Cy3 channel. Merge: Cy3 channel and bright filed. Scale bar: 50 μm. **c** The binding ability analysis of ZAJ4a, 7D12 and ZAJ4a-7D12 by flow cytometry. **d** The last frame snapshot of EGFR/PTPRF/ZAJ4a-7D12 complex on membrane surface. EGFR, 7D12, PTPRF and ZAJ4a were colored in green, red, cyan and orange, respectively. The lipid bilayer was represented by black sticks. **e** Contact area of EGFR and 7D12, PTPRF and ZAJ4a in the system of EGFR/PTPRF/ZAJ4a-7D12 complex. **f** RMSD of each part of the complex. Both 7D12 and PTPRF were components of ZAJ4a-7D12. **g** Schematic illustration of ZAJ4a-7D12 induced artificial protein-proximity on the cell membrane. **h** Dual-color TIRF images of EGFR-mNeongreen (green) and PTPRF-Tdtomato (red). Scale bar: 5 μm. **i** Pearson's correlation coefficients of EGFR-mNeongreen and PTPRF-Tdtomato. Data are obtained from Fig. 2h by using ImageJ software ($n = 3$ independent experiments). Data are shown as means ± SD, and p-values are determined by one-way ANOVA with Tukey's multiple comparisons test in (**i**). The exact p-values are shown in the figure. Source data are provided as a Source Data file.

EGFR, as a representative model. EGFR is a widely distributed RTK protein and plays a key role in pathological conditions such as cancer. The aptamer ZAJ4a (sequence showed in Supplementary Table 1) was selected to recruit phosphatase PTPRF, as it showed high binding affinity (Kd in the nanomolar range) to PTPRF[17]. The nanobody 7D12 was utilized as a binder for EGFR with the amino acid sequence modified according to previous studies (Supplementary Table 2)[18]. To construct a heterobifunctional Apt-PRC ZAJ4a-7D12, 7D12 was modified with NH_2-PEG_3-N_3 under the catalysis of microbial transglutaminases (MTG), and then conjugated to DBCO-modified aptamer ZAJ4a (ZAJ4a-DBCO) by click chemistry reaction (Supplementary Fig. 1). The successful conjugation of 7D12 with ZAJ4a was confirmed by polyacrylamide gel electrophoresis (PAGE). Compared to the single 7D12 (~15 kDa, Fig. 2a, lane 2), a new band at approximately 32 kDa emerged in lane 3 (Fig. 2a), indicating the successful construction of covalent ZAJ4a-7D12. To assess the binding ability of ZAJ4a-7D12, SACC-83 cells expressing both PTPRF and EGFR (Supplementary Fig. 2) were treated

with ZAJ4a, 7D12 or ZAJ4a-7D12, respectively, and then visualized under a confocal laser scanning microscope (CLSM). We found ZAJ4a, 7D12 and ZAJ4a-7D12 could successfully bind to the corresponding target membrane proteins (Fig. 2b). In contrast, negligible fluorescence was shown in SACC-83 cells with random DNA treatment (Supplementary Fig. 3, left), and in K562 cells (EGFR-negative cells) with 7D12 treatment (Supplementary Fig. 3, middle) or with random DNA-7D12 treatment (Supplementary Fig. 3, right). This was consistent with flow cytometry analysis results, demonstrating the dual targeting capability of ZAJ4a-7D12 (Fig. 2c). To further investigate the binding specificity of the two moieties of the ZAJ4a-7D12 on their respective receptors, we selected two different single-positive cell lines, MCF-7 cells (EGFR − /PTPRF +) and HCT116 cells (EGFR + /PTPRF −), as determined through immunofluorescence staining (Supplementary Fig. 4a, b). Living cells were treated with ZAJ4a, 7D12 and ZAJ4a-7D12. Intense fluorescent signals were occurred in MCF-7 cells with ZAJ4a and ZAJ4a-7D12 incubation, and in HCT116 cells with 7D12 and ZAJ4a-

7D12 incubation, but negligible fluorescence was observed in MCF-7 cells with 7D12 incubation and HCT116 cells with ZAJ4a incubation (Supplementary Fig. 4c, d). These findings confirmed that the two moieties of the ZAJ4a-7D12 could act independently on the two different receptors. Consistently, we observed that under the same conditions, the ZAJ4a-7D12 exhibited superior targeting capabilities toward SACC-83 cells compared to ZAJ4a alone, and similar binding ability with 7D12 alone (Supplementary Fig. 5).

Based on experimental results, we employed molecular docking and all-atomistic MD simulations to investigate the binding modes of 7D12 and ZAJ4A with their related proteins. Notably, the extracellular domain of EGFR could hold the 7D12 like a palm (Supplementary Fig. 6a). Their interactions were dominated by hydrogen bonds, which preserved the stability of the interaction interface (Supplementary Fig. 6b). Considering the large extracellular domain of PTPRF, we firstly confirmed the probable binding domains of the aptamer ZAJ4a within PTPRF by constructing a series of truncated plasmids of PTPRF, which were transfected into 293 T cells, and then treated with ZAJ4a-Cy3. The results showed that the domain Ig1-3 of PTPRF played an essential role in the binding process (Supplementary Fig. 6c). The Ig1-3 region of PTPRF intertwines with ZAJ4A, and the major groove of ZAJ4A fits snugly, locking the Ig1-3 domains in place (Supplementary Fig. 6d). The binding process between PTPRF and ZAJ4a was mainly driven by the electrostatic interactions (Supplementary Fig. 6e). These salt bridges ensured robust binding of the complex. The RMSD analysis shows that the structural fluctuations of these biomolecules are relatively small (Supplementary Fig. 6f), indicating that the binding of ZAJ4A and 7D12 to the target proteins is stable.

It is noteworthy that the motion behavior of membrane proteins on the cell membrane is complex. For PTPRF, the Ig1-3 region only a part of its extracellular domain. To further explore the interactions between the Apt-PRC ZAJ4a-7D12 and related proteins on the cell membrane surface, we constructed coarse-grained (CG) models and performed CGMD simulations. The extracellular region of PTPRF is a linear structure composed of multiple domains connected sequentially, with the Ig1-3 region located at the distal end of this structure (Supplementary Fig. 6g). After ZAJ4a-7D12 binds to the Ig1-3 region of PTPRF, it also forms nonspecific interactions with other regions of PTPRF under the guidance of electrostatic interactions (Supplementary Fig. 6h). The RMSD of PTPRF indicates that these interactions could restrict the structural flexibility of PTPRF (Supplementary Fig. 6i), thereby reducing the degrees of freedom of the extracellular region of PTPRF. This may enhance the probability of interaction between the chimera and EGFR.

Moreover, we investigated the motion behavior of EGFR on the membrane (Supplementary Fig. 6j–l). We calculated the distance between the centroid of the extracellular region of EGFR and the membrane surface (Supplementary Fig. 6m). The CGMD simulations revealed that EGFR exhibited a swaying motion on the membrane surface. The binding of the 7D12 monomer to EGFR did not alter this motion. In contrast, when ZAJ4a-7D12 bound to EGFR, the swaying tendency of EGFR was reduced. The nucleic acid chain in ZAJ4a-7D12 carried negative charge, which could form electrostatic interactions with the positively charged head groups of lipids. This anchoring effect restricted the motion of EGFR, resulting in a larger contact area between the 7D12 and EGFR (Supplementary Fig. 6n). This indicated that the binding between the ZAJ4a-7D12 and EGFR is more stable. Notably, this enhancement in binding stability was independent of the nucleic acid sequence. When the nucleic acid in the chimera was replaced with a random sequence (named random DNA-7D12), the motion of EGFR was similarly restricted (Supplementary Fig. 6m, n).

In addition, we examined the interactions among the ZAJ4a-7D12, PTPRF and EGFR on the membrane surface (Fig. 2d). Simulations indicated that the ZAJ4a-7D12 could bind to both PTPRF and EGFR simultaneously. The contact area between 7D12 and ZAJ4a with their

target proteins indicated that the interactions within the complex were stable (Fig. 1e). With the assistance of ZAJ4a-7D12, the two membrane proteins gradually approach each other. This observation demonstrated that the two proteins could directly form a complex on the cell membrane under the induction of the ZAJ4a-7D12. During the process of EGFR approaching and interacting with PTPRF, the structure of EGFR remained largely stable (Fig. 2f). In contrast, the relative positions of the domains within PTPRF underwent changes, leading to greater RMSD fluctuations. However, these structural fluctuations did not affect the binding between the PTPRF and ZAJ4a-7D12. The RMSD analysis showed that the structure of ZAJ4A remained unchanged, indicating that the PTPRF/ZAJ4A complex retained structural stability.

Having demonstrated the successful conjugation and the robust binding of ZAJ4a-7D12, we next investigated whether they could force two target proteins into close proximity on the same cell membrane. A dual-color single molecule total internal reflection fluorescence (TIRF) microscope was used to detect the colocalization of PTPRF and EGFR proteins. SACC-83 cells were co-transfected with Tdtomato tagged PTPRF (PTPRF-Tdtomato) and mNeongreen tagged EGFR (EGFR-mNeongreen) (Fig. 2g). The TIRF imaging showed that PTPRF-Tdtomato and EGFR-mNeongreen signals appeared as well-dispersed fluorescent spots on cell membrane without any treatment (Fig. 2h, control). In contrast, a significant overlap of PTPRF-Tdtomato and EGFR-mNeongreen signals was observed after the treatment of ZAJ4a-7D12, but not ZAJ4a or 7D12 (Fig. 2h and Supplementary Fig. 8). To quantify the correlation between PTPRF and EGFR, Pearson's correlation coefficients (PCCs) were calculated as previously described[19]. The PCC of the ZAJ4a-7D12 group was calculated as 0.82, much higher than the other three groups, demonstrating the strong colocalization of PTPRF and EGFR (Fig. 2i). These results suggested that Apt-PRCs ZAJ4a-7D12 worked successfully as molecular mediators to draw PTPRF and EGFR closer together on the cell membrane. It is noted that the control group showed a PCC of ~0.4, reflecting a weak linear relationship between the two proteins. This observation is consistent with recent studies reporting a limited interaction between PTPRF and EGFR[20,21]. Together, these findings provide a foundation for future research exploring forced proximity of PTPRF and EGFR through chimeric constructs. To further confirm the influence of ZAJ4a-7D12 on the EGFR dimerization, A549 ells with relatively low expression of EGFR[22] were assessed as previously described[23]. A549 cells were transfected with EGFR-mNeongreen and treated with ZAJ4a-7D12 or monovalent counterpart in the presence or absence of EGF. Based on the calculations, ~87.9% and ~12.1% of EGFR were monomers and homodimers, respectively, in the transfected A549 cells (Supplementary Fig. 9, control). Upon EGF stimulation, the homodimer proportion increased to ~38.4% (Supplementary Fig. 9b, EGF). Notably, ZAJ4a-7D12 effectively suppressed the EGFR homodimerization to ~21.13% (Supplementary Fig. 9b, ZAJ4a-7D12), while ZAJ4a or 7D12 alone treatment exhibited negligible inhibitory effects. These findings suggested that ZAJ4a-7D12 competitively inhibited the formation of EGFR homodimers from monomers, which in turns contributed to the formation of EGFR-PTPRF heterodimers.

Apt-PRCs recruited PTPRF to dephosphorylate EGFR
Given that Apt-PRCs ZAJ4a-7D12 enforced the close proximity of PTPRF to EGFR (Fig. 3a), we evaluated whether they could modulate receptor phosphorylation and subsequent intracellular downstream signaling. First, the dephosphorylation effect of ZAJ4a-7D12 was assessed in SACC-83 cells. EGF was used to reconstitute EGFR phosphorylation in SACC-83 cells. Western blot analysis was conducted to check the EGFR phosphorylation (pEGFR) level after treatment with ZAJ4a, 7D12, or ZAJ4a-7D12, respectively. Neither ZAJ4a nor 7D12 induced observable changes in pEGFR levels, whereas pEGFR expression noticeably decreased following treatment with ZAJ4a-7D12 (Fig. 3b, c). To further investigate whether ZAJ4a-7D12 reduced EGFR
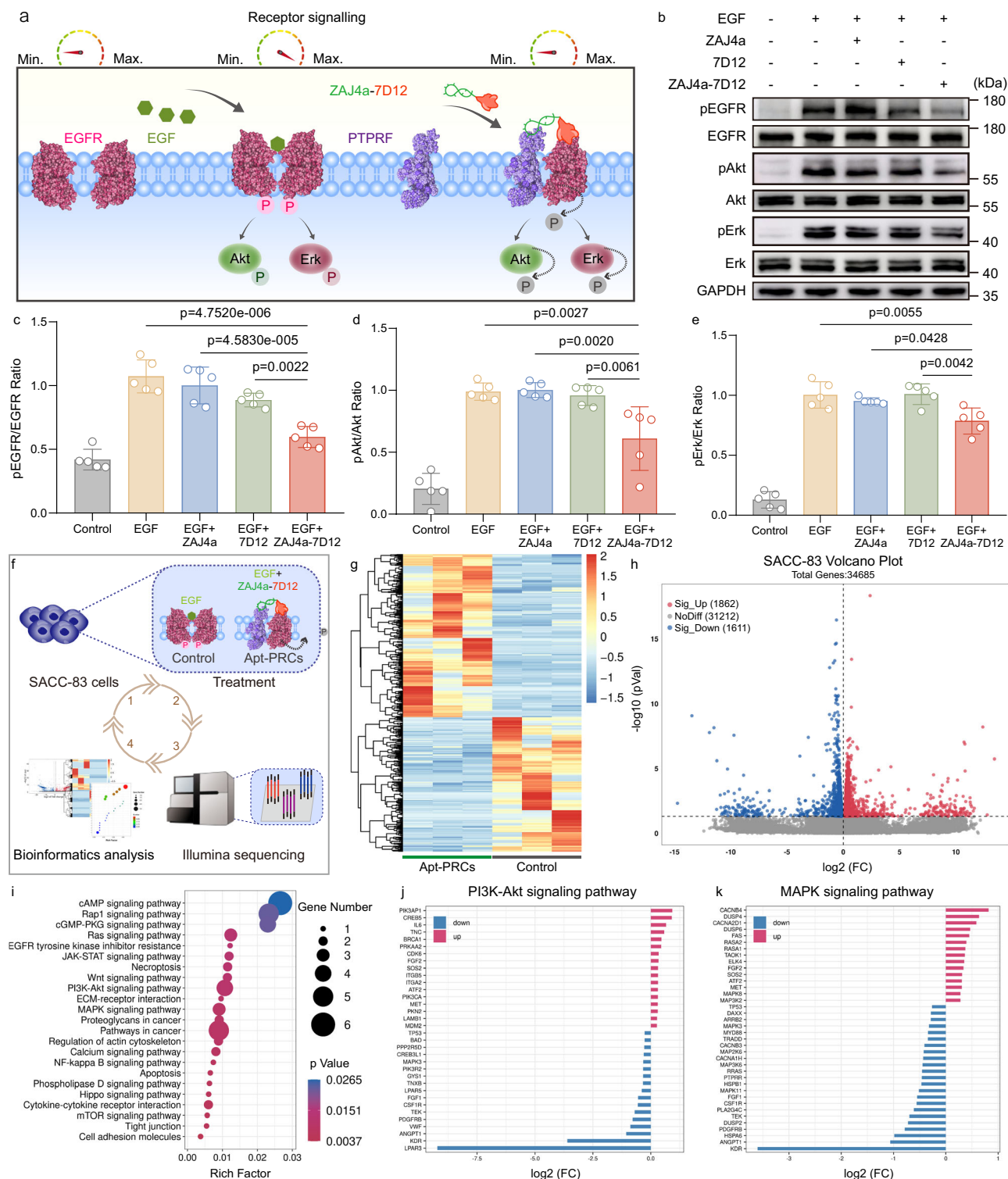
Fig. 3 | Apt-PRCs recruited PTPRF to dephosphorylate EGFR. a Schematic illustration of artificial protein-proximity of phosphatases and membrane receptors, enforced by ZAJ4a-7D12, to regulate signaling pathways. **b** Dephosphorylation effects of ZAJ4a-7D12 determined by western blot in SACC-83 cells. The pEGFR levels were detected at Y1068. Uncropped blots were provided in Source Data. **c**–**e** Semi-quantification of pEGFR expression level (**c**) pAkt expression level (**d**) and pErk expression level (**e**) by calculating the western blot band intensity ratio of the phosphorylation protein to total proteins using ImageJ software ($n = 5$ independent experiments). **f** Schematic illustration of cell transcriptional responses upon treatment with ZAJ4a-7D12. **g** The heatmap of DEGs in the SACC-83 cells treated with ZAJ4a-7D12 plus EGF

(Apt-PRCs group, green) or EGF alone (control group, gray) ($n = 3$ independent samples). **h** The volcano plot of the up- and down-regulated DEGs in the Apt-PRCs group compared to the control group. Blue and red dots indicate significant changed genes in the Apt-PRCs group, with $p < 0.05$ and $|\log_2(FC)| > 0$. **i** KEGG pathway enrichment analysis of DEGs in SACC-83 cells. **j**, **k** Changes of genes enriched in PI3K-Akt signaling pathway (**j**) and MAPK signaling pathway (**k**). $n = 3$ independent samples. Data are shown as means ± SD, and p-values are determined by unpaired two-tailed Student's t-test in (**h**), one-way ANOVA with Tukey's multiple comparisons test in (**c**–**e**) and one-sided Fisher exact test with Benjamini-Hochberg adjustment in (**i**). The exact p-values are shown in the figure. Source data are provided as a Source Data file.

signal transduction in SACC-83 cells, we examined the major down-stream signaling proteins after ZAJ4a-7D12 treatment. As expected, ZAJ4a-7D12 significantly downregulated the levels of pAkt and pErk (Fig. 3b, d and e). As a contrast, monovalent ZAJ4a or 7D12 had minimal effects on dephosphorylation of pEGFR, pAkt and pErk (Fig. 3b–e). To validate the necessity of PTPRF in dephosphorylation, we constructed the PTPRF-knockdown SACC-83 cells using PTPRF siRNA. The disappearance of PTPRF band indicated the successful knockdown of PTPRF at the concentration of exceeding 50 nM (Supplementary Fig. 10a, b). Subsequently, the PTPRF-knockdown cells were treated with EGF for 10 min, followed by treatment with ZAJ4a, 7D12, or ZAJ4a-7D12. The dephosphorylation effect of ZAJ4a-7D12 significantly diminished in PTPRF-knockdown cells (Supplementary Fig. 10c–g), underscoring the fundamental involvement of PTPRF in dephosphorylation. To further confirm the dephosphorylated site influenced by ZAJ4a-7D12, we assessed the dephosphorylation levels of EGFR at multiple tyrosine residues, including Y1173, Y1148, Y1086, Y1068, Y1045, Y998, Y992, and Y845, in SACC83 cells. The results indicated significant dephosphorylation effects at all of these phosphorylated sites (Supplementary Fig. 10h–p). The combined treatment of unconjugated ZAJ4a and 7D12 showed barely decrease of EGFR dephosphorylation induced by EGF, which further confirmed that dephosphorylation effects were dependent on the proximity of PTPRF and EGFR enforced by ZAJ4a-7D12.

To further evaluate the modulation of ZAJ4a-7D12 in EGFR function, the transcriptional responses were examined using RNA-sequencing method (Fig. 3f). In detail, SACC-83 cells treated with EGF alone for 24 h were set as the control group, and cells treated with ZAJ4a-7D12 in the presence of EGF were set as the Apt-PRCs group. Differentially expressed genes (DEG) analysis revealed the robust transcriptional responses in both groups (Fig. 3g). Compared to the control group, the Apt-PRCs group showed upregulation of 1,862 genes and downregulation of 1,611 genes ($p < 0.5$, $|\log_2 FC| \geq 0$) (Fig. 3h). Kyoto Encyclopedia of Genes and Genomes (KEGG) analysis was conducted to identify potential pathways involved in DEGs, such as PI3K-Akt and MAPK (also known as Erk) signaling pathways related to cancer (Fig. 3i). Indeed, genes enriched in PI3K-Akt and MAPK signaling pathways were differentially affected (Fig. 3j and k), consistent with the variation tendency of dephosphorylation levels induced by ZAJ4a-7D12 (Fig. 3b). Therefore, Apt-PRCs ZAJ4a-7D12 can be customized to modulate EGFR phosphorylation levels to regulate different transcriptional responses. Collectively, these data demonstrated that the as-constructed Apt-PRCs ZAJ4a-7D12 enabled the accurate regulation of EGFR dephosphorylation and subsequent intracellular downstream signaling by promoting the enforced proximity of EGFR and PTPRF.

Apt-PRCs regulated cell behaviors

Considering that EGF-stimulated hyperactivation of EGFR could promote unregulated cell proliferation and migration via Akt and Erk signaling[24], we subsequently explored the impact of Apt-PRCs ZAJ4a-7D12 on cell behaviors. We first evaluated their capacity to inhibit the growth and proliferation of SACC-83 cells. CCK-8 assay was performed to determine the viability of SACC-83 cells upon treatment with 100 ng/mL EGF followed by different concentrations of ZAJ4a, 7D12 and ZAJ4a-7D12. Compared with the other three groups, ZAJ4a-7D12 significantly decreased cell viability in a dose-dependent manner (Fig. 4a). Next, we confirmed that ZAJ4a-7D12 promoted cell apoptosis by Annexin V-FITC and PI (AV/PI) staining (Fig. 4b and Supplementary Fig. 11a). To investigate the effect of ZAJ4a-7D12 on cell-cycle progression, cellular DNA content was determined using PI staining by flow cytometric analysis. The results showed that ZAJ4a-7D12 disturbed cell cycle and induced dramatic arrest in S phase (Fig. 4c and Supplementary Fig. 11b). The increase of cell proportion in S phase was accompanied by a concomitant reduction of cell proportion in G2/M

phase of the cell cycle, indicating the inhibition of mitotic progression and cell survival. However, these phenomena were not observed in cells treated with ZAJ4a or 7D12 in the presence of EGF. Cell migration can be promoted by EGF signaling, which is also related to cancer cell metastasis. Considering the metastatic characteristics of SACC-83 cells, we examined behavioral features of cell migration. Wound healing assay was conducted to demonstrate the mobility of SACC-83 cells under different conditions. The cells with ZAJ4a-7D12 treatment exhibited a much lower degree of wound closure than that with treatment of ZAJ4a or 7D12 (Fig. 4d and Supplementary Fig. 12a). Particularly, compared to EGF only treatment, the addition of ZAJ4a-7D12 led to a ~1.7-fold rise in the area of wound gap after 12 h (Supplementary Fig. 12b).

Since epithelial-mesenchymal transition (EMT) is known to play a pivotal role in cancer metastasis associated with the EGFR pathway[24], we further studied whether ZAJ4a-7D12 could influence the EMT pathway. A hallmark of EMT is the downregulation of E-cadherin and the upregulation of Vitmentin[25]. Western blot analysis revealed that only ZAJ4a-7D12 treatment, not the others, reversed the loss of E-cadherin and the gain of Vimentin induced by EGF (Fig. 4e–g). This observation suggested that ZAJ4a-7D12 may inhibit cell migration by potentially interfering with the EMT pathway. To gain a deeper understanding of ZAJ4a-7D12 on EMT, we examined the transcriptional responses through RNA-sequencing. Specifically, we examined EMT-related genes from the database for epithelial-mesenchymal transition genes version 2.0 (dbEMT 2.0, http://dbemt.bioinfo-minzhao.org/index.html) in SACC-83 cells[26]. The heatmap with differentially expressed gene (DEG) analysis displayed the robust transcriptional responses in both groups (Fig. 4h). The volcano plots of DEG analysis showed 520 upregulated and 523 down-regulated EMT-related genes in Apt-PRCs group compared to the control group (Fig. 4i). Notably, the eight most significantly altered EMT hallmark genes ($p < 0.05$ and $|\log_2(FC)| > 1$) were displayed in Fig. 4j, providing a probable explanation for the mitigation of EMT features. In conclusion, Apt-PRCs ZAJ4a-7D12 effectively regulated cell behaviors associated with proliferation, migration and phenotypic transition by modulating EGFR receptor function.

Apt-PRCs-induced dephosphorylation enhanced gefitinib response in EGFR^{T790M}-mutated PC9/GR cells in vitro and in vivo

Drug resistance is a worldwide healthcare crisis that impedes disease treatment and increases financial burden[27]. EGFR TKIs, including gefitinib, erlotinib and afatinib, are effective as first-line treatment for advanced non-small-cell lung cancers (NSCLC). However, acquired resistance of TKI is nearly inevitable after a progression-free period of approximately 8–12 months[28]. Given the successful regulation of EGFR dephosphorylation and cell behaviors achieved through the Apt-PRCs strategy, we anticipated that ZAJ4a-7D12 could potentially combat drug resistance in EGFR TKI-resistant NSCLC cells. In gefitinib-resistant cells, EGFR mutation sterically hinders the binding of gefitinib to the ATP-binding site of the EGFR tyrosine kinase domain, inducing its autophosphorylation and constitutive activation of the intracellular signaling cascades. The abnormal signaling pathway triggered the drug resistance (Fig. 5a, left).

Herein, we applied the Apt-PRCs strategy to drive enforced proximity of EGFR and PTPRF, dephosphorylate the EGFR, attenuate the intracellular signaling cascades, and thus, in turn, improve gefitinib treatment efficacy in resistant cells (Fig. 5a, right). Proof-of-concept assays were conducted on gefitinib-resistant PC9 cells (PC9/GR cells). First of all, we detected the EGFR mutational status in PC9/GR cells through whole exome sequencing. The data showed that PC9/GR cells harbored small in-frame deletions in exon 19 and T790M mutation in exon 20 (Supplementary Fig. 13). These genetic changes acted as oncogenic drivers causing ligand-independent constitutive activation of EGFR downstream signaling, and thus promoting cell proliferation,
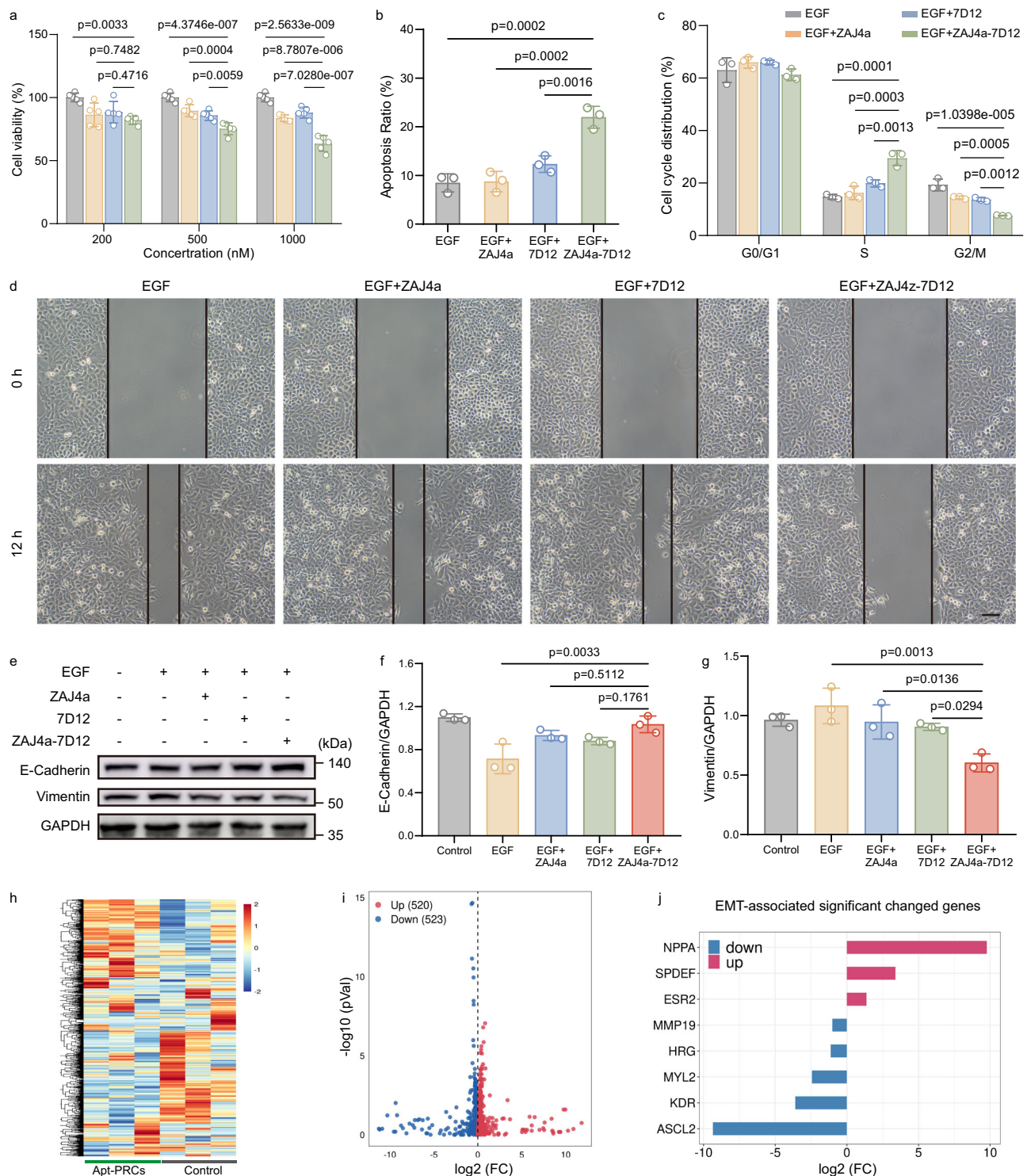
Fig. 4 | Apt-PRCs regulated cell behaviors and transcriptional responses. a Cell viability analysis of SACC-83 cells by CCK-8 assay (*n* = 5 independent experiments). **b** Apoptosis analysis of SACC-83 cells stained by AV/PI (*n* = 3 independent experiments). **c** Cell cycle distribution analysis of SACC-83 cells stained by PI solutions (*n* = 3 independent experiments). **d** Representative images of wound healing in SACC-83 cells with different treatment. Scale bar: 100 μm. **e** Expression levels of E-Cadherin and Vimentin determined by western blot. Uncropped blots were provided in Source Data. **f, g** Semi-quantification of E-Cadherin expression level (**f**) and Vimentin expression level (**g**) by calculating the western blot band intensity ratio of the protein to GAPDH using ImageJ software (*n* = 3 independent

experiments). **h** The heatmap of EMT-related DEGs in the SACC-83 cells treated with ZAJ4a-7D12 plus EGF (Apt-PRCs group, green) or EGF alone (control group, gray) (*n* = 3 independent samples). **i** The volcano plot of changed DEGs in the Apt-PRCs group compared to the control group. **j** Significantly changed genes associated with EMT in the Apt-PRCs group compared to the control group. Data are shown as means ± SD, and *p*-values are determined by one-way ANOVA with Tukey's multiple comparisons test in (**a**–**c**, **f**, **g**) and unpaired two-tailed Student's *t*-test in (**i**). The exact *p*-values are shown in the figure. Source data are provided as a Source Data file.
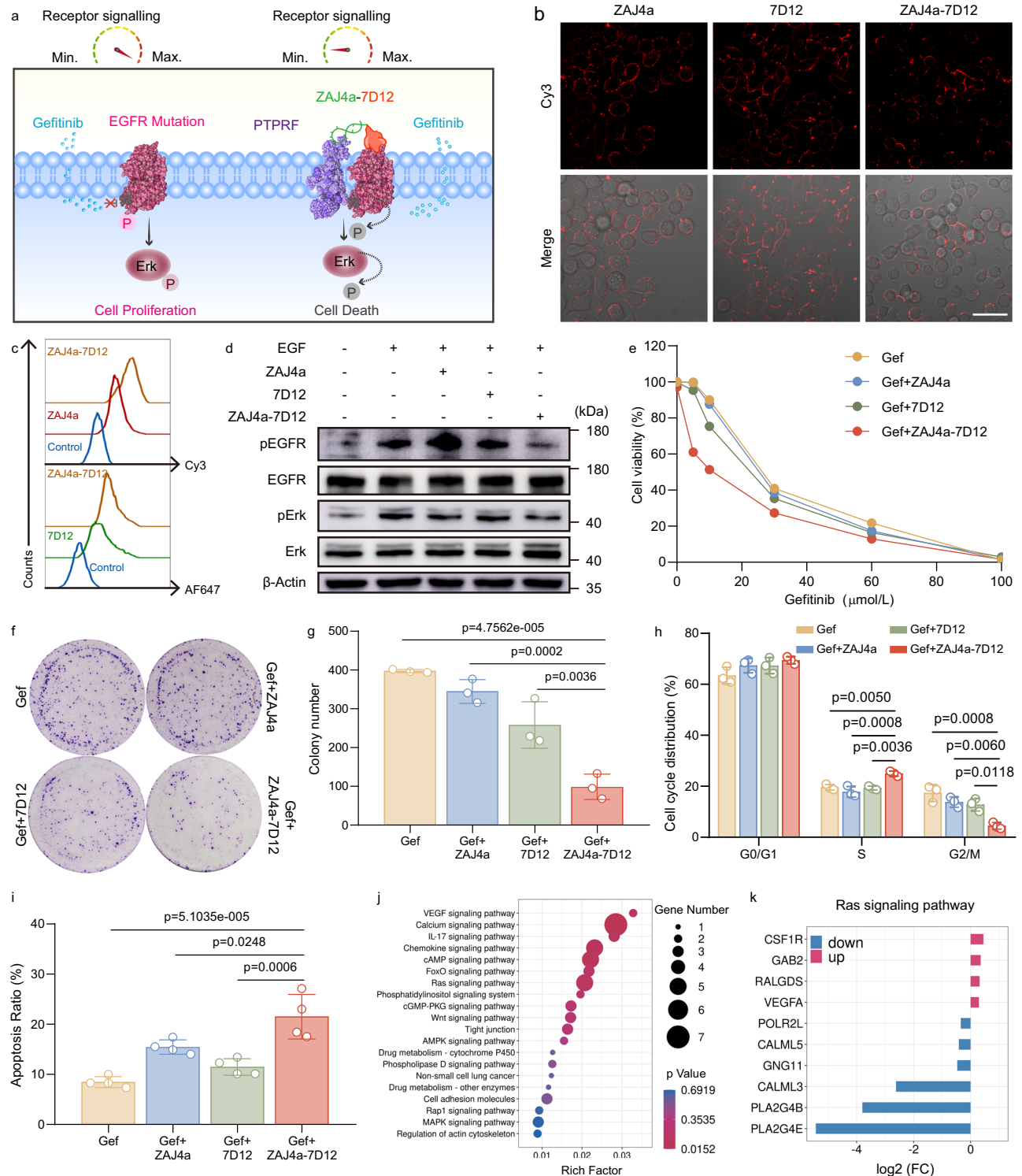
Fig. 5 | Apt-PRCs ZAJ4a-7D12 enhanced gefitinib response in EGFR[T790M]-mutated PC9/GR cells. a Schematic illustration of ZAJ4a-7D12 enhancing the susceptibility of PC9/GR cells to gefitinib. **b**, **c** The binding ability analysis of ZAJ4a, 7D2 and ZAJ4a-7D12 to PC9/GR cells verified by CLSM (**b**) and flow cytometry (**c**). Scale bar: 50 μm. **d** Dephosphorylation effects of ZAJ4a-7D12 determined by western blot in PC9/GR cells. Uncropped blots were provided in Source Data. **e** Gefitinib IC50 values of PC9/GR cells with different treatments calculated by CCK-8 assay. **f** Colony formation assay of PC9/GR cells. **g** Statistical analysis of colony number in PC9/GR cells ($n = 3$ independent experiments). **h** Cell cycle distribution analysis of PC9/GR cells stained by PI solutions ($n = 4$ independent experiments). **i** Apoptosis analysis of PC9/GR cells using AV/PI staining by flow cytometry ($n = 3$ independent experiments). **j** KEGG pathway enrichment analysis of DEGs in PC9/GR cells. **k** Changes of genes enriched in Ras signaling pathway. The gefitinib concentration used in 4e-4k was 5 μM. Data are shown as means ± SD, and p-values are determined by one-way ANOVA with Tukey's multiple comparisons test in (**g**–**i**) and one-sided Fisher exact test with Benjamini-Hochberg adjustment in (**j**). The exact p-values are shown in the figure. Source data are provided as a Source Data file.
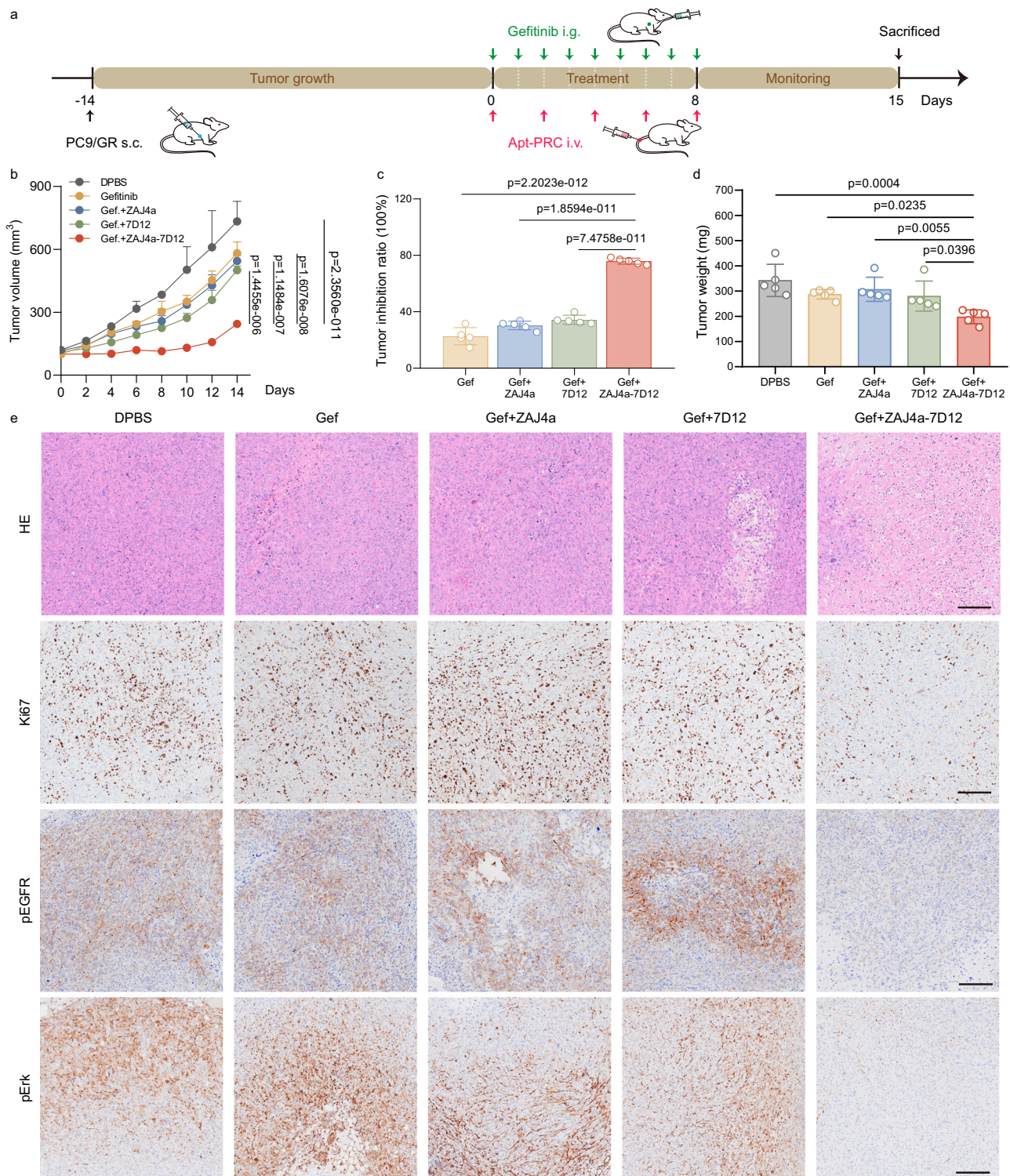
Fig. 6 | ZAJ4a-7D12 treatment enhanced gefitinib efficacy in gefitinib-resistant tumor bearing mice. a Schematic illustration of therapeutic schedule in gefitinib-resistant tumor bearing mice. **b** The tumor growth curve ($n = 5$ mice). **c** The tumor growth inhibition ratio ($n = 5$ mice). **d** Tumor weight variation ($n = 5$ mice). **e** Representative images of H&E staining and immunohistochemical staining of Ki-67, pEGFR and pErk of tumors isolated from mice after different treatments ($n = 3$ mice). Scale bar: 200 μm. Data are shown as means ± SD, and p-values are determined by one-way ANOVA with Tukey's multiple comparisons test in (**b**–**d**). The exact p-values are shown in the figure. Source data are provided as a Source Data file.

survival and migration[29]. Next, we confirmed the successful recognition of ZAJ4a-7D12 to PC9/GR cells through CLSM imaging and flow cytometry analysis (Fig. 5b, c). To evaluate the dephosphorylation effects of ZAJ4a-7D12 on EGFR in PC9/GR cells, the dephosphorylation levels were assessed after treatment with EGF for 30 min followed by ZAJ4a, 7D12 or ZAJ4a-7D12 for another 30 min. Compared to ZAJ4a or 7D12 treatment, ZAJ4a-7D12 significantly elevated the dephosphorylation levels of pEGFR as well as the downstream signaling effectors pErk in the presence of EGF (Fig. 5d and Supplementary Fig. 14). To assess the susceptibility to gefitinib, PC9/GR cells were

treated with gefitinib (Gef), gefitinib plus ZAJ4a (Gef+ZAJ4a), gefitinib plus 7D12 (Gef+7D12) or gefitinib plus ZAJ4a-7D12 (Gef+ZAJ4a-7D12), and the corresponding IC50 values were calculated as 27.45 μM, 25.06 μM, 21.05 μM and 9.26 μM, respectively. Remarkably, ZAJ4a-7D12 induced leftward shifts in the gefitinib dose-response curves and reduced IC50 values for growth inhibition, indicating alleviation of gefitinib resistance (Fig. 5e). To investigate the relationship between 7D12-ZAJ4a and gefitinib in treatment, we determined their combination effects using the CCK-8 assays. The results indicated that the combination treatment more effectively inhibited cell growth compared to gefitinib alone or 7D12-ZAJ4a alone (Supplementary Fig. 15a, b). Furthermore, we conducted a classic isobologram analysis for the combination effect of gefitinib and ZAJ4a-7D12 according to previously reported methods[30,31]. Both the green and red dots of combination treatment fell on the lower left, indicating the potential synergistic effect of the ZAJ4a-7D12 with gefitinib (Supplementary Fig. 15c).

At the same time, ZAJ4a-7D12 inhibited colony formation of PC9/GR cells in the presence of gefitinib, highlighting a significant restoration of gefitinib susceptibility compared to the control groups (Fig. 5f, g). Moreover, ZAJ4a-7D12 induced obvious changes in cell cycle distribution in the presence of gefitinib, as confirmed through PI staining and flow cytometry analysis. Our results revealed that the cells treated with ZAJ4a-7D12 experienced a shift in the cell cycle from G2/M to S phase compared to the control groups, suggesting an interference with cell mitosis and growth (Fig. 5h and Supplementary Fig. 16a). As expected, cell apoptosis ratio induced by ZAJ4a-7D12 was much higher than the control groups (Fig. 5i and Supplementary Fig. 16b). Taken together, ZAJ4a-7D12 attenuated EGFR/Erk signaling pathway and interrupted malignant behavior of gefitinib-resistant cancer cells, demonstrating excellent capability to modulate EGFR function and to overcome EGFR^T790M-associated drug resistance.

To further understand the downstream signaling pathway modulated by ZAJ4a-7D12, we conducted a comprehensive analysis of the cell transcriptomes in PC9/GR cells through RNA-sequencing. The KEGG pathway enrichment analysis of DEGs highlighted notable alterations in major signaling pathways, such as the Ras signaling pathway, calcium signaling pathway, and chemokine signaling pathway (Fig. 5j). In a more focused examination of specific genes within these pathways, we observed that Gef+ZAJ4a-7D12 treatment was associated with the enrichment of numerous gene sets related to the Ras signaling pathway (Fig. 5k). Ras functions as a pivotal element at the core of the EGFR signaling pathway[32]. Positioned upstream in the Ras/Raf/MEK/Erk axis, it can be activated by phosphorylated EGFR, leading to the ineffectiveness of EGFR-targeted therapies[33]. Considering the alteration of Ras signaling pathway in combining the reduced levels of pErk shown above (Fig. 5d), we speculated that ZAJ4a-7D12 modulated EGFR function and its signal transduction. Such findings in PC9/GR cells demonstrated that ZAJ4a-7D12 restrained the EGFR signaling pathway through dephosphorylation, thereby enhancing the susceptibility to gefitinib. This suggested the great potential of Apt-PRCs to overcome gefitinib resistance induced by EGFR^T790M mutation.

To further evaluate whether ZAJ4a-7D12 could enhance the susceptibility of PC9/GR cells to gefitinib in vivo, a therapeutic study was conducted using a subcutaneous gefitinib-resistant NSCLC tumor-bearing mouse model. Mice inoculated with PC9/GR cells were treated with DPBS, gefitinib (Gef), gefitinib plus ZAJ4a (Gef+ZAJ4a), gefitinib plus 7D12 (Gef+7D12) or gefitinib plus ZAJ4a-7D12 (Gef+ZAJ4a-7D12) after the tumors reached approximately 100 mm3 (n = 5 mice per group) (Fig. 6a). First, to assess the systemic safety profiles of ZAJ4a-7D12, hematoxylin and eosin (H&E) examination of main organs from mice did not reveal any obvious change between the Gef+ZAJ4a-7D12 group and the other control groups (Supplementary Fig. 17a). As well, there was no significant body weight loss observed in mice throughout the duration of study, demonstrating excellent biocompatibility of Gef

+ZAJ4a-7D12 (Supplementary Fig. 17b). Regarding the anti-tumor effects, gefitinib alone had only a minor effect on inhibiting the growth of PC9/GR tumors (Fig. 6b, c and Supplementary Fig. 8c). However, Gef+ZAJ4a-7D12 treatment efficiently arrested tumor growth, with an inhibition ratio of 72.71%, whereas the Gef+ZAJ4a group and the Gef+7D12 group were inhibited by 28.39% and 31.33%, respectively (Fig. 6b–d and Supplementary Fig. 17c). Histological examination of H&E staining was carried out for comparing morphology changes of tumor cells after different treatments. The tumor cells from the DPBS group had a large nucleus and spindle shape, indicating rapid tumor proliferation. The morphological features of partial necrosis were displayed in the Gef, Gef+ZAJ4a and Gef+7D12 groups. In contrast, obvious decrease in tumor cellularity, nuclei shrinkage and the largest area of necrosis occurred in the Gef+ZAJ4a-7D12 group (Fig. 6e). Ki-67 staining was conducted to investigate further the behavioral feature of cell proliferation. It was found that Ki-67 staining was widespread in tumors from the DPBS group as well as the monotherapy group, but significantly reduced in the Gef+ZAJ4a-7D12 group (Fig. 6e and Supplementary Fig. 18a). The results indicated ZAJ4a-7D12 efficiently inhibited cell proliferation in gefitinib-resistant tumors. In addition, we observed that ZAJ4a-7D12 treatment led to a more significant effect on inhibiting tumor growth in vivo than that on promoting cell apoptosis in vitro. It implied that the mechanism of growth inhibition may involve pathways beyond apoptosis. Our RNA sequencing results revealed that ZAJ4a-7D12 treatment induced alterations in several signaling pathways, including calcium signaling, chemokine signaling, and IL-7 signaling (Fig. 5j), which were associated with tumor growth as previously reported[34,35]. These findings suggested that the observed growth inhibition may be attributed to a complex interplay of factors influencing tumor growth, rather than being solely dependent on apoptosis.

Having demonstrated that ZAJ4a-7D12 enhanced susceptibility to gefitinib in resistant tumor bearing mice, we further investigated whether this was achieved through dephosphorylation of EGFR and the downstream signaling proteins. Immunohistochemical analysis showed that Gef + ZAJ4a-7D12 significantly increased the dephosphorylation levels of pEGFR, as well as downstream signaling proteins pErk, while limited dephosphorylation was observed in the other groups (Fig. 6e and Supplementary Fig. 18b, c). These results clearly indicated that ZAJ4a-7D12 exerted a substantial therapeutic effect in inhibition of gefitinib-resistant xenograft growth in mice, mainly by accelerating the dephosphorylation of EGFR and modulating its function.

Application of Apt-PRCs to diverse membrane receptors

Given the substrate promiscuity of PTPRF and its widespread expression in cancer cells[15], we postulated that the Apt-PRCs could be readily applicable to other membrane receptors of interest. Met, known as a driver of tumor development and progression with high abundance on membranes, was chosen as another membrane receptor (Fig. 7a). Aptamer SL1 was used as a binder to specifically recognize Met. The Apt-PRC ZAJ4a-SL1 is formed by linking ZAJ4a and SL1 via a double-stranded nucleic acid linker (Supplementary Table 1 and Supplementary Fig. 19). The successful construction of ZAJ4a-SL1 was confirmed by 12% native PAGE (Supplementary Fig. 20a). CLSM and flow cytometry analysis were used to verify the specificity of ZAJ4a-SL1 to PTPRF and Met in Lovo cells (Supplementary Fig. 20b, c). After ZAJ4a-SL1 treatment, the colocalization of PTPRF and Met proteins on the cell membrane was evidenced by TIRF imaging and PCCs quantification (Supplementary Fig. 21a, b). We next examined the dephosphorylation effects of ZAJ4a-SL1 by western blot analysis. ZAJ4a-SL1 indeed promoted the dephosphorylation of Met and its downstream signaling proteins pAkt and pErk in the presence of hepatocyte growth factor (HGF), but not monovalent ZAJ4a, SL1 or HGF only treatment (Fig. 6b and Supplementary Fig. 22).
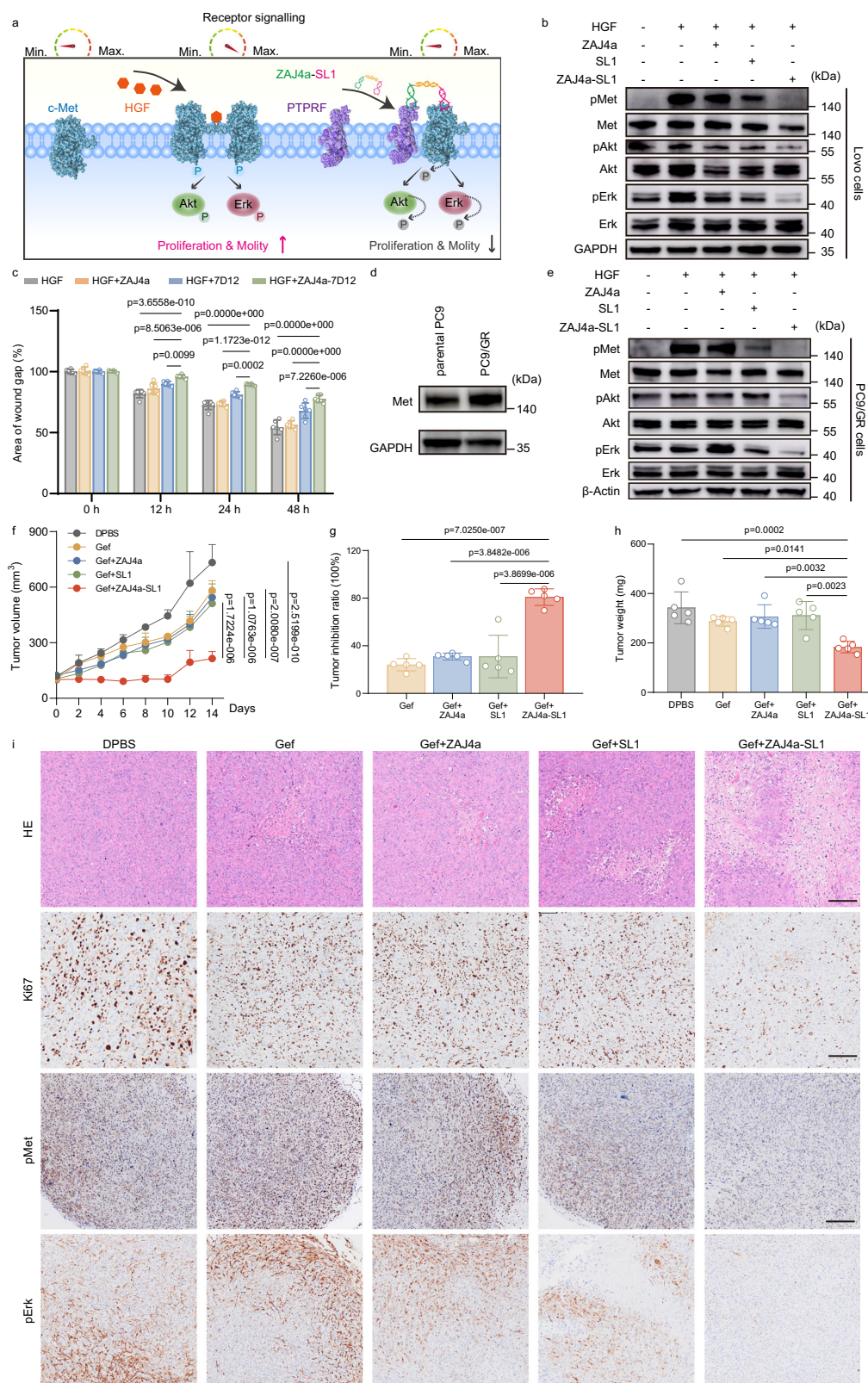
Fig. 7 | Apt-PRCs promoted dephosphorylation of diverse membrane receptors. a Schematic illustration of Apt-PRCs ZAJ4a-SL1 action mechanism. **b** Dephosphorylation effects of Apt-PRCs ZAJ4a-SL1 determined by western blot in Lovo cells. **c** Quantitative acellular area of wound healing assay ($n = 5$ independent experiments). **d** Western blot analysis of Met expression levels in parental PC9 cells and PC9/GR cells. **e** Western blot analysis of pMet, pAkt and pErk expression levels in PC9/GR cells with different treatments. **f** The tumor growth curve ($n = 5$ mice). **g** The tumor growth inhibition ratio ($n = 5$ mice). **h** Tumor weight variation ($n = 5$ mice). **i** Representative images of H&E staining and immunohistochemical staining of Ki-67, pMet and pErk of tumors isolated from mice after different treatments. Scale bar: 200 μm. Data are shown as means ± SD, and p-values are determined by two-way ANOVA with Tukey's multiple comparisons test in (**c**) and one-way ANOVA with Tukey's multiple comparisons test in (**f–h**). The exact p-values are shown in the figure. Uncropped blots of (**b–e**) were provided in Source Data. Source data are provided as a Source Data file.

Next, we evaluated the impact of ZAJ4a-SL1 on cell behaviors. CCK-8 assay and AV/PI staining confirmed that ZAJ4a-SL1 significantly inhibited the proliferation and promoted the apoptosis of Lovo cells in the presence of HGF (Supplementary Fig. 23a–c). Cell proliferation and apoptosis are intimately coupled with the receipt of appropriate mitogenic signals[36]. Cell cycle analysis showed ZAJ4a-SL1 caused an accumulation of the Lovo cells in S phase, with the percentages increased by 18.23 to 26.83% after 48 h treatment, thereby decreasing the proportion of cells in G2/M phase (Supplementary Fig. 23d, e). That implied disruption of cell cycle and inhibition of mitosis. Furthermore, wound healing assay demonstrated that ZAJ4a-SL1 inhibited cell migration in Lovo cells (Fig. 7c and Supplementary Fig. 24). These effects were not observed or less significant with the ZAJ4a or SL1 treatment. Collectively, these results illustrated that the Apt-PRCs ZAJ4a-SL1 can effectively inhibit cell proliferation and migration by regulating Met dephosphorylation.

The Met signaling pathway is another compensatory feedback loop that mostly arises during the treatment of TKI. In addition to EGFR^{T790M} mutations, Met protein overexpression has long been recognized as a key mechanism underlying gefitinib resistance and is detectable in approximately 5–22% of NSCLC patients with acquired resistance to first-generation EGFR-TKIs[37,38]. As well, we found PC9/GR cells had higher levels of Met protein expression compared to parental PC9 cells (Fig. 7d). Phosphorylation of Met induces the activation of Akt and Erk cascades to rescue tumor cells from TKI[39]. Thus, we investigated whether Apt-PRCs ZAJ4a-SL1 could enhance susceptibility to gefitinib through modulation of the bypassing signaling pathway. Firstly, western blot analysis in vitro revealed ZAJ4a-SL1, rather than monotherapy, could downregulate pMet/pAkt/pErk signaling pathway in PC9/GR cells (Fig. 7e and Supplementary Fig. 25). To further determine the effects of ZAJ4a-SL1 in vivo, we conducted therapeutic treatment in gefitinib-resistant NSCLC tumor bearing mouse model. Mice were treated with DPBS, gefitinib (Gef), gefitinib plus ZAJ4a (Gef +ZAJ4a), gefitinib plus SL1 (Gef+SL1) or gefitinib plus ZAJ4a-SL1 (Gef + ZAJ4a-SL1), respectively, after tumor reached approximately 100 mm3 ($n = 5$ mice per group). H&E stains of mice organs and stable body weight confirmed the safety profiles and biocompatibility property of ZAJ4a-SL1 (Supplementary Fig. 26a and 26b). Strikingly, the tumor growth profiles displayed dramatic decrease of tumor volume in the Gef + ZAJ4a-SL1 group, with the inhibition ratio of 79.03%, higher than that of other groups (Fig. 7f–h and Supplementary Fig. 26c). For pathologic analysis, H&E staining showed that tumor tissues of Gef + ZAJ4a-SL1 treated mice were distinctive from the other groups, characterized by extensive nuclei shrinkage and histological structures with loose tissue gaps (Fig. 7i). Similarly, immunohistochemical analysis of Ki67 also showed Gef+ZAJ4a-SL1 existed apparent anti-tumor effects compared to other treatments (Fig. 7i and Supplementary Fig. 27a). As well, we confirmed ZAJ4a-SL1 promoted dephosphorylation of pMet and downstream effectors pErk to combat gefitinib resistance (Fig. 7i and Supplementary Fig. 27b, c). Collectively, these encouraging results verified Apt-PRCs ZAJ4a-SL1 could efficiently blocked bypass signaling in resistant tumors and sensitized the PC9/GR cells to gefitinib by modulating Met protein function.

In consideration of the satisfactory results in both Gef+ZAJ4a-7D12 and Gef+ZAJ4a-SL1 treatment, we further explored the effect of ZAJ4a-7D12 alone, ZAJ4a-SL1 alone and in combination. The in vitro effects on cell growth in PC9/GR cells were detected by CCK-8 assays. The exposure to the combined treatment induced a stronger inhibitory effect, at concentrations as low as 500 nM, compared to individual treatment with ZAJ4a-7D12 or ZAJ4a-SL1 (Supplementary Fig. 28a). Furthermore, we assessed the combination effect of ZAJ4a-7D12 and ZAJ4a-SL1 on tumor growth in vivo. Similar to the animal experiments described above (Fig. 6a), gefitinib-resistant NSCLC tumor bearing mice were treated with ZAJ4a-7D12 alone, ZAJ4a-SL1 alone and in combination. H&E stains of mice organs confirmed the safety profiles

and biocompatibility property of all these treatments (Supplementary Fig. 29). The tumor volume and weight were significantly suppressed in the combination treatment as compared to the individual treatment (Supplementary Fig. 28b–28d). Meanwhile, both H&E staining and immunohistochemical staining of Ki-67 indicated robust anti-tumor effects of the combination treatment (Supplementary Fig. 30a and d). To further explore the mechanism underlying the combination treatment-mediated inhibitory effect, we examined EGFR signaling pathways. The dephosphorylations of pEGFR, pMet and pAkt were significantly observed in the combination treatment (Supplementary Fig. 30). These findings implied that the combined treatment ZAJ4a-7D12 and ZAJ4a-SL1 is an alternative strategy for gefitinib-resistant treatment.

Discussion

In summary, we developed aptamer-directed phosphatase recruiting chimeras to achieve precise and effective dephosphorylation regulation of diverse membrane receptors. Taking advantage of the recognition and binding ability of aptamers and nanobodies, Apt-PRCs enforced artificial proximity of phosphatase PTPRF and specific membrane receptors, i.e., EGFR and Met, followed by editing dephosphorylation status of the membrane receptors and regulating downstream signaling pathways. In consideration of this, Apt-PRCs presented great capacity in controlling cell behaviors like proliferation, migration and phenotypic transition by manipulating receptor function.

Of note, Apt-PRCs strikingly enhanced susceptibility to gefitinib in PC9/GR cells, showing great potential in alleviating even overcoming the drug resistance. Broadly, it is intriguing that modulating signal transduction is sufficient to affect their susceptibility to drugs. The RAS/RAF/MEK/ERK and PI3K/PTEN/AKT axes are the main downstream signaling pathways of EGFR. Upregulated other RTKs, including Met, activate the Akt axis and/or the Erk pathway independently of EGFR as a compensatory feedback loop signaling[40]. Alterations in these pathways, such as gene mutation, gene amplification, gene loss and abnormal phosphorylation, carry profound implications in resistance to TKI. Herein, EGFR^{T790M} mutation and activated Met bypass pathway induced abnormal downstream signaling could be turned off by Apt-PRCs in the presence of EGFR-TKI in vitro and in vivo. Through manipulating the phosphorylation status of EGFR and Met, we managed to improve the gefitinib treatment efficacy in PC9/GR cells and PC9/GR cell-bearing mice. The Apt-PRC thus is a promising tool to abrogate hyperactivated signaling to combat drug resistance. We believe that Apt-PRC is versatile strategy and could be used to overcome the problem of drug resistance in more types of cancers. Actually, this is a growing area of interest as multiple recent studies showed that phosphorylation status of signal effectors can globally change both cellular behavior and susceptibility to target drugs[41,42].

Moreover, we confirmed that Apt-PRCs could recruit non-native protein-enzyme partners. Given the existence of diverse cell-surface membrane receptors that are expressed on different cell types, the Apt-PRCs strategy potentially affords the possibility of specific receptor inhibition for a wide range of kinase-linked receptors. We currently managed to achieve the dephosphorylation of only two representative membrane receptors, EGFR and Met, and future efforts will focus on more cancer targets. Taken together, Apt-PRC represents a general strategy for direct attenuation of signaling by kinase-activated membrane receptors, and offers a promising approach to promote the advancement of targeted cancer therapy.

Methods

Ethics statement

This study complies with all relevant ethical and safety regulations. The animal experiments were approved by the Animal Ethics Committee of Hangzhou Institute of Medicine (HIM), Chinese Academy of Sciences

(approval document number: 2023R022) and were performed in a facility accredited by the Association for the Assessment and Accreditation of Laboratory Animal Care. The maximal tumor burden is 10% body weight set by the Animal Ethics Committee of HIM. Throughout all experiments, tumor burden was maintained within the limits.

Expression and purification of 7D12

The pET22b expression vector and E. coli BL21 (DE3) were purchased from Sangon Biotech (Shanghai) Co., Ltd. and Vazyme Biotech Co.,Ltd., respectively. The amino acid sequence of 7D12 was listed in supplementary Table 1.7D12 gene was optimized and synthesized by General Biosystems Co. Ltd. The positive clone was propagated in Luria–Bertani medium containing 100 µg/mL of ampicillin at 37 °C overnight with constant shaking at 200 rpm. Subsequently, the overnight culture was diluted in Terrific-Broth (TB) medium and then shaken at 37 °C with 200 rpm. When the OD600 value reached 0.6–0.8, iso-propyl β-D-thiogalactoside was added to induce target protein expression at 16 °C for another 24 h. After the fermentation completed, cells were harvested by centrifugation and then resuspended in lysis buffer (10 mmol/L Tris-HCl, 300 mmol/L NaCl, pH = 7.8) After disruption on ice by sonication, the supernatant was collected by centrifugation and incubated with Ni–NTA agarose on ÄKTA avant system. Thereafter, the agarose was washed with 20 mM imidazole to remove other proteins. The N-terminal 6×His-tagged target proteins were then eluted from the agarose with 300 mM imidazole and finally desalted using a HiPrep Desalting column on ÄKTA avant system. The concentrations of the target proteins were determined using BCA kit.

Conjugation of nanobody 7D12 and aptamer ZAJ4a

Aptamer ZAJ4a was conjugated to nanobody 7D12 through transamidation reaction catalyzed by MTG and click chemistry reaction. In brief, 7D12 in balance buffer (dulbecco's phosphate-buffered saline, DPBS, pH 7.4, Corning, USA) was mixed with NH_2-PEG_3-N_3 (50 eq. relative to 7D12) and catalyzed by 1 U/mL MTG at room temperature for 8 h. Afterwards, the production was purified by Ni sepharose (17526801, Cytiva, USA) in spin column (C006724, Sangon Biotech, China) with 20 mM imidazole (288-32-4, Aladdin, China) in balance buffer to remove the excess of NH_2-PEG_3-N_3 and MTG, following washing with 300 mM imidazole to collect production. The production was further buffer-exchanged to balance buffer by 15 mL Amicon® Ultra Centrifugal Filters with a MWCO of 10 kDa (Merck/EMD Millipore, France) to remove the imidazole. The concentration of 7D12-N_3 was measured by BCA Protein Assay Kit (Beyotime, China). Then, DBCO-modified ZAJ4a was diluted with DPBS at 100 µM, and mixed with 7D12-N_3 (0.625 eq. relative to ZAJ4a-DBCO) at 4 °C overnight. The purification procedures were the same as described above. The concentration of ZAJ4a-7D12 was measured by Nanodrop (Thermo Fisher Scientific, USA) and the purity was analyzed by 4–20% SurePAGE™ (Genscript, China).

Construction of bispecific aptamer ZAJ4a-SL1

ZAJ4a-linker (ZAJ4a-L) and SL1-linker* (SL1-L*) ssDNA strands were mixed together at the molar ratio of 1:1 and were annealed at 95 °C for 5 min, followed by cooled down on ice for 30 min to form ZAJ4a-SL1 bispecific construction. 12% native PAGE in 1×TBE buffer was used to validate the formation of ZAJ4a-SL1.

Cell Culture

Lovo (Catalog # CCL-229), MCF-7 (Catalog # HTB-22), HCT116 (Catalog # CCL-247), A549 (Catalog # CCL-185) cells were purchased from American Type Culture Collection (ATCC), PC9 and PC9/GR cells were gifts from Zhejiang Cancer Hospital. SACC-83 cells were gifts from the laboratory of Prof. Tao Bing (Hangzhou Institute of Medicine, Chinese Academy of Sciences). All cells were cultured in RPMI 1640 medium supplemented with 10% fetal bovine serum, 1% penicillin–streptomycin solution (100 µg/mL), and were cultured in a humidified incubator containing 95% air and 5% CO_2 at 37 °C.

The all cell lines used in this study have been authenticated by Short Tandem Repeat (STR) analysis, conducted by Shanghai Biowing Applied Biotechnology Co., Ltd., and all results confirmed their identity (Supplementary Data 1–7). Additionally, mycoplasma contamination was tested using the Mycoplasma PCR Detection Kit (C0301S, Beyotime, China), and no contamination was detected in any of the cell lines (Supplementary Data 8).

Confocal microscopic imaging of cells labeled by Apt-PRCs

SACC-83, Lovo and PC9/GR cells were seeded in a glass-bottom dish and maintained at 37 °C in 5% CO_2 overnight. After washing twice with DPBS, SACC-83 and PC9/GR cells were incubated with ZAJ4a-Cy3, 7D12 or ZAJ4a-Cy3-7D12 for 30 min at room temperature for 20 min. Subsequently, cells conjugated with 7D12 were stained with CoraLite®594-conjugated anti-His antibody for another 30 min. Lovo cells were stained with ZAJ4a-L-Cy3, SL1-L*-Cy5 or ZAJ4a-Cy3-SL1-Cy5 for 20 min at room temperature. Finally, the labeled cells were washed twice with DPBS and imaged by A1 HD25 confocal microscope (Nikon, Japan).

Flow cytometric analysis of cells labeled by Apt-PRCs

Cells were detached from the culture dish with TrypLE Express (Gibco, USA) after being washed with DPBS. SACC-83 and PC9/GR cells were incubated with ZAJ4a-Cy3, 7D12 or ZAJ4a-Cy3-7D12 for 20 min at room temperature. Subsequently, cells conjugated with 7D12 were stained with CoraLite® Plus 647-conjugated anti-His antibody for another 30 min. Lovo cells were stained with ZAJ4a-L-Cy3, SL1-L*-Cy5 or ZAJ4a-Cy3-SL1-Cy5 for 20 min at room temperature. After being washed 3 times with DPBS, the labeled cells were detected on CytoFLEX (Beckman Coulter Life Sciences, USA) by counting 10000 events. FlowJo software (V 10.8.1) was used for data analysis.

Truncated PTPRF expression on the cell membrane

The amino acid sequence of PTPRF was acquired from the open access online database UniProt (https://www.uniprot.org/uniprotkb/P10586/entry). The extracellular domain of PTPRF consisted of three immunoglobulin-like domains (Ig1-3), eight fibronectin type III (FNIII) domains (FN1-8). Therefore, five truncated plasmids were designed, named D2 (Ig1-3 deletion), D3 (Ig1-3 and FN1-2 deletion), D4 (Ig1-3 and FN1-4 deletion), D5 (Ig1-3 and FN1-6 deletion), D6 (Ig1-3 and FN1-8 deletion). The untruncated plasmids were named D1. The cDNA of PTPRF was constructed into the vector pcDNA3.1EGFP. The recombinant plasmids were synthesized and purchased from Anhui General Biol. The detailed sequences and information of truncated PTPRF were listed in Table S3.

All these plasmids were transfected into 293 T cells, followed by treatment with 500 nM ZAJ4a-Cy3 or random strands for 20 min at room temperature. The labeled cells were detected on CytoFLEX (Beckman Coulter Life Sciences, USA) by counting 10000 events. FlowJo software (V 10.8.1) was used for data analysis.

Structure modeling

The 3D structure of EGFR (extracellular domain and transmembrane domain, 25 ~ 668) was derived from the crystal structure of EGFR (PDB ID: 1IVO (25-646)). The Alphafold2 database was employed to fix the missing structure. The 3D structural models of the EGFR nanobody were sourced from the crystal structure of 7D12 in combination with domain III of the extracellular portion of EGFR (PDB ID: 4KRL). This structure was also used to construct the complex model of the EGFR-7D12.

The 3D structure of PTPRF (extracellular domain and transmembrane domain, 30 ~ 1284) was derived from the crystal structure of PTPRF (PDB ID: 2YD5 (29-231); 2DJU (319-411); 6TPW (319-706);

2EDX (596-716); 2DN7 (821-914); 2EDY (915-1010)). The Alphafold2 database was employed to fix the missing structure. The 3D structural models of the PTPRF aptamer ZAJ4A were predicted using the previously reported in silico protocol[43]. Based on the sequence information provided by the experiments, we used the HADDOCK 2.4 server to dock ZAJ4A with PTPRF Ig1-3 domain and constructed the PTPRF-ZAJ4A complex model[44]. For the bispecific EGFR-PTPRF chimeric system, a small linker was covalent connected to the ZAJ4a (DA56, phosphate group) and 7D12 (Q150, amide group on the side chain). The small molecular linker was built using the VMD 1.9.3 software. The length of the linker is 2.9 nm, which is greater than the non-bonded interaction cutoff.

All-atomic simulations

We utilized all-atomic simulations to examine the binding stability of the EGFR/7D12 and PTPRF/ZAJ4a complexes. For the simulation system of EGFR/7D12, we added a POPC lipid bilayer to the system using CHARMM-GUI webserver. Since the binding region of ZAJ4a with PTPRF (residues 30-314) is far from the transmembrane region (residues 1264-1284), we did not include a lipid bilayer in the simulation. All the simulation boxes were hydrated with 0.99 g/ml water. The TIP3P model was employed to reproduce the bulk water. The 0.15 M NaCl was added into water to neutralized the charge of biomolecules. The periodic boundary conditions (PBC) were employed on all three dimensions.

The MD simulations were performed in the NPT ensemble using the Gromacs2022.5 software with the GPU acceleration[45]. The Charmm36 force field (ver. 2021july) was used for the biomolecule systems[46]. A cutoff value of 1.1 nm was used to treated the nonbonded interactions. The Particle Mesh Ewald (PME) algorithm was used to compute long-range electrostatic interactions[47]. For the EGFR/7D12 system, the pressure coupling was maintained at 1 bar using semi-isotropic coupling with the Parrinello-Rahman barostat with a coupling constant of $\tau p = 2$ ps. The temperature was controlled at 310 K by the Nose-Hoover algorithm using a coupling constant of $\tau t = 0.5$ ps. For the PTPRF/ZAJ4a system, pressure coupling was maintained at 1 bar using isotropic coupling with the Parrinello-Rahman barostat with a coupling constant of $\tau p = 2$ ps. The temperature was controlled at 310 K by the Nose-Hoover algorithm using a coupling constant of $\tau t = 0.5$ ps. All simulations started with a 5000-step energy minimization using steepest descent gradient algorithm. Before production runs all systems were equilibrated for 10 ns. Finally, 500 ns-long productive MD simulations were carried out for data collection. The time step for the all-atom MD simulation was 2 fs. The was RMSD employed to evaluate the structural stability of the biomolecules.

The criteria for identifying a hydrogen bond XH···Y are as follows: a. The distance between the heavy atoms X and Y is less than 3.5 nm; b. The X-H-Y angle is greater than 150 degrees[48].

Coarse-grained simulations

To evaluate the stability of different complexes, we employed coarse-grained (CG) simulations to examine their behaviors on the cell membrane (Supplementary Fig. 7). The 3D structure of EGFR, 7D12, PTPRF, and ZAJ4A were converted to a coarse-grained model using the Martinize.py script[49]. An ELNEDYN network was applied to the protein using a force constant of 500 kJ/mol/nm2 and a cut off of 1.5 nm[50]. The small molecule linker was constructed following the MARTINI2 protocol (https://cgmartini.nl/docs/tutorials/Legacy/martini2/parametrizing.html).

Furthermore, the insane.py script (download from https://cgmartini.nl/docs/downloads/tools/proteins-and-bilayers.html) was utilized to insert the membrane proteins into the POPC (1-palmitoyl-2-oleoyl-sn-glycero-3-phosphocholine) lipid bilayer[51]. The entire simulation system was filled with Martini water beads, and neutralized to a concentration of 0.15 M NaCl.

All CGMD simulations were implemented using the GROMACS v.2022 simulation package. Simulations were performed as an NPT ensemble, with temperature maintained at 310 K using a v-rescale thermostat using a coupling constant of $\tau t = 1$ ps, and semi-isotropic pressure controlled at 1 bar using a parrinello-rahman barostat with a coupling constant of $\tau p = 12$ ps and a compressibility of 3×10^{-4} bar^{-1} [52]. Electrostatics were modeled using the reaction field coulomb type, and smoothly shifted between 0 and 1.1 nm[53]. Van der Waals interactions were treated using a shifting function between 0.9 and 1.1 nm. Covalent bonds were constrained to their equilibrium values using the LINCS algorithm[54]. All the simulation boxes were energy minimized for 100000 steps using the steepest descent algorithm. After energy minimization, equilibrium runs were performed for 5 ns with a 1 fs time step. Finally, production MD was simulated for 500 ns with a 2 fs time step.

We used gmx sasa to calculate the contact area between biomolecules. First, we calculated the solvent accessible surface area (SASA) of the biomolecular complex (S1). Then, we calculated the SASA of the two individual biomolecules separately (S2 and S3). The contact area was determined as (S2 + S3-S1)/2. Moreover, we used g_select to select the backbone of the extracellular domain of EGFR and calculated its centroid coordinate along the z-axis (z1). For the cell membrane, the position of the membrane surface (z2) was defined as the average z-axis coordinate of the POPC head groups. The distance between the extracellular domain of EGFR and the membrane surface was determined as z1-z2.

Single molecule fluorescence imaging

The SACC-83 cells were co-transfected with mNeongreen-EGFR and Tdtomato-PTPRF. The Lovo cells were co-transfected with mNeongreen-Met and Tdtomato-PTPRF. The plasmids were constructed as previous reported[19]. Transfection was performed using Lipofectamine 3000 transfection reagent (Invitrogen, USA) according to the manufacturer's instructions. The single molecule fluorescence images were performed on an Olympus Cell TIRF microscope equipped with a total internal reflective fluorescence illuminator, a x 100/1.5 NA plan apochromatic TIR objective and a scientific complementary metal-oxide-semiconductor camera (sCMOS). The mNeongreen and Tdtomato tagged samples were excited at 488 and 561 nm of lasers, respectively.

For colocalization assays, after 10 h transfection, the SACC-83 and Lovo cells were incubated with ZAJ4a-7D12 and ZAJ4a-SL1 for 30 min, respectively. After being washed 3 times with DPBS, cells were fixed in 4% paraformaldehyde for 20 min at room temperature. The colocalization were analyzed with Colocalization plug-in of ImageJ software (National Institutes of Health).

For analysis of the proportion between monomer and dimer, the A549 cells were co-transfected with mNeongreen-EGFR. After 8 h transfection, A549 cells treated with EGF, followed by ZAJ4a, 7D12 or ZAJ4a-7D12 treatment. The fluorescence intensity of each protein spot was assessed by ImageJ software. Frequency distributions of the fluorescence intensities were generated with OriginPro 10. The histogram of the fluorescent intensities was fitted by the sum of two Gaussian functions.

Western blot analysis

To detect the dephosphorylation effect of ZAJ4a-7D12 on EGFR protein, SACC83 and PC9/GR cells were plated in the 6-well plates (4×10^5 cells per well) cultured at 37 °C with 5% CO_2 for 24 h. After serum starved for 24 h, SACC-83 and PC9/GR cells were treated with 10 ng/mL and 30 ng/mL EGF for 30 min, respectively. ZAJ4a-7D12 was added for another 30 min incubation at 37 °C. To detect the dephosphorylation effect of ZAJ4a-SL1, Lovo and PC9/GR cells were treated with 50 ng/mL HGF for 30 min after seeding for 24 h and starvation for another 24 h at 37 °C. Subsequently, ZAJ4a-SL1 was

added for another 30 min incubation at 37 °C. To validate the necessity of PTPRF in dephosphorylation, PTPRF siRNA (siPTPRF) with different concentrations were used to construct the PTPRF-knockdown SACC-83 cells. Negative control siRNA (siNC) was used as control. The sequences of siPTPRF and siNC were lisited in Supplementary Table 4. Tthe results showed that the concentration of siPTPRF at 50 nM was enough to knockdown the PTPRF in SACC-83 cells (Supplementary Fig. 10a). Subsequently, the PTPRF-knockdown cells were treated with EGF for 10 min, followed by treatment with 500 nM ZAJ4a, 7D12, or ZAJ4a-7D12 for 30 min.

After treatment, RIPA lysis buffer (Applygen Technologies, China) containing protease inhibitor cocktail, phosphatase inhibitor cocktail I and II (MedChemExpress, USA) was used to extract total proteins. Protein concentration of each cell lysate was measured by BCA Protein Assay Kit. Total proteins were resolved with 4–20% SurePAGE™ and blotted onto a polyvinylidene difluoride membrane (Millipore, USA). The membranes were blocked with no protein blocking solution (Sangon Biotech, China) for 2 h at room temperature and probed with the following primary antibodies at 4 °C overnight: anti-phospho-EGFR (Y1068) (1:1000, ET1612-30, HUABIO, China), anti-EGFR (1:1000, ET1604-44, HUABIO, China), anti-phospho-Met (Tyr1234/1235) (1:1000, #3077, CST, USA), anti-Met (1:1000, #8918, CST, USA), anti-phospho-Akt (Ser473) (1:1000, #9271, CST, USA), anti-Akt (1:1000, #9272, CST, USA), anti-phospho-Erk (Thr202/Tyr204) (1:1000, #4370, CST, USA), anti-Erk (1:1000, #4695, CST, USA), anti-E-Cadherin (1:1000, #14472, CST, USA), anti-Vimentin (1:1000, #5741, CST, USA), anti-β-actin (66009-1-Ig, Proteintech, China) and anti-GAPDH (60001-1-Ig, Proteintech, China) antibody, anti-phospho-EGFR (Y1173) (1:1000, #4407, CST, USA), anti-phospho-EGFR (Y1148) (1:1000, #4404, CST, USA), anti-phospho-EGFR (Y1086) (1:1000, #2220, CST, USA), anti-phospho-EGFR (Y1045) (1:1000, #2237, CST, USA), anti-phospho-EGFR (Y998) (1:1000, #2641, CST, USA), anti-phospho-EGFR (Y992) (1:1000, #2235, CST, USA), anti-phospho-EGFR (Y845) (1:1000, #6963, CST, USA). After washing 3 times with TBST, the membranes were incubated with horseradish peroxidase-conjugated secondary antibodies (SA00001-1, SA00001-2, Proteintech, China) for 1 h at room temperature. Protein bands were visualized by incubation with Super ECL Plus (Applygen Technologies, China) and scanned by Amersham ImageQuant 800 Imager (Cytiva, Japan). Densitometry was performed by using the ImageJ software (National Institutes of Health, USA).

CCK-8 assay
Cells (1×10^4) were seeded onto 96-well plates and incubated for 24 h at 37 °C. For cell proliferation assay, SACC-83 and Lovo cells were serum starved for 24 h. SACC-83 cells were treated with 100 ng/mL EGF and various concentrations of ZAJ4a, 7D12 or ZAJ4a-7D12 for 24 h. Lovo cells were treated with 50 ng/mL HGF and various concentrations of ZAJ4a, SL1 or ZAJ4a-SL1 for 24 h. For determination of IC50 values, PC9/GR cells were exposed to various concentrations of gefitinib and 500 nM ZAJ4a, 7D12 or ZAJ4a-7D12 for 24 h. Subsequently, the mixture of 10 μL CCK-8 (Applygen Technologies, China) and 100 μL medium was added to each well and incubated for 45 min-1 h. Measure the absorbance at 450 nm using the SPARK® multimode microplate reader (Tecan, Swiss). The IC50 values were calculated by GraphPad Prism 8.0 software (GraphPad Software, USA).

Colony formation assay
PC9/GR cells (1×10^3) were plated in 6 well plates containing 5 μM gefitinib with 500 nM ZAJ4a, 7D12 or ZAJ4a-7D12 and cultured at 37 °C under 5% CO_2 undisturbed for 14 days. The medium was changed every 7 days with the indicated drugs. After 14 days of culture, cells were fixed with 4% paraformaldehyde, and then stained with 0.5% crystal violet for 20 min and washed 3 times with DPBS. Plates were air-dried and imaged by Amersham ImageQuant 800 Imager.

Apoptosis analysis and cell cycle analysis
All cells (4×10^5) were seeded onto 6-well plates and incubated for 24 h at 37 °C. After 24 h serum starvation, SACC-83 cells were treated with 500 nM ZAJ4a, 7D12 or ZAJ4a-7D12 in the presence of 10 ng/mL EGF, and Lovo cells were treated with 50 nM ZAJ4a, SL1 or ZAJ4a-SL1 in the presence of 50 ng/mL HGF. PC9/GR cells were treated with 500 nM ZAJ4a, 7D12 or ZAJ4a-7D12 in the presence of 5 μM gefitinib. For apoptosis analysis, the medium was collected and cells were detached from the culture dish with TrypLE Express after 48 h treatment. The collected cells were proceeded with Annexin V-FITC&PI Apoptosis Detection Kit (Sangon Biotech, China) according to the manufacturer's instructions. The cells were washed twice with DPBS and then resuspended in 195 μL 1 × binding buffer. 5 μL annexin V-FITC was added to incubate with cells for 15 min at room temperature protected from light. After washing in 200 μL 1 × binding buffer, cell resuspension was centrifuged to discard supernatant. The cells were resuspended in 190 μL 1 × binding buffer and incubated with 10 μL propidium iodide (PI) for 15 min at room temperature in the dark. For cell cycle analysis, cells were detached from the culture dish with TrypLE Express after 48 h treatment and fixed with 70% ethanol overnight at 4 °C. After washing with DPBS, cells were then incubated with 50 μg/mL propidium iodide containing RNaseA (Yuanye, China) in dark at 37 °C for 30 min. The apoptosis assay and cell cycle assay were analyzed using CytoFLEX. The data were compensated and analyzed using FlowJo software (V 10.8.1).

Wound healing assay
SACC-83 (8×10^3) and Lovo (1×10^4) cells were seeded into each chamber of the Culture-Insert (Ibidi, Germany) until they form an optically confluent monolayer. The Culture-Insert was removed after 24 h serum starvation to create a defined cell-free gap of 500 μm. SACC-83 cells were treated with 500 nM ZAJ4a, 7D12 or ZAJ4a-7D12 in the presence of 100 ng/mL EGF. Lovo cells were treated with 50 nM ZAJ4a, SL1 or ZAJ4a-SL1 in the presence of 200 ng/mL HGF. Images of wounded areas were captured by inverted phase contrast microscope at different time points and area of wound gap was determined by ImageJ software (NIH, USA).

RNA sequencing and bioinformatics analysis
SACC-83 and PC9/GR cells were seeded onto 6-well plates and incubated for 24 h at 37 °C. After 24 h serum starvation, SACC-83 cells were treated with 500 nM ZAJ4a-7D12 in the presence of 10 ng/mL EGF as the Apt-PRCs group, and that treated with 10 ng/mL EGF alone acted as the control group. PC9/GR cells were treated with 500 nM ZAJ4a-7D12 in the presence of 5 μM gefitinib as the Apt-PRCs group, and that treated with 5 μM gefitinib alone acted as the control group. The medium was changed every 12 h with the indicated drugs. After 24 h treatment, total RNA was extracted using Trizol reagent (Thermo Fisher, 15596018) following the manufacturer's procedure. The total RNA quantity and purity were analysis of Bioanalyzer 2100 and RNA 6000 Nano LabChip Kit (Agilent, CA, USA, 5067-1511), high-quality RNA samples with RIN number > 7.0 were used to construct sequencing library. After total RNA was extracted, mRNA was purified from total RNA (5 ug) using Dynabeads Oligo (dT) (Thermo Fisher, CA, USA) with two rounds of purification. Following purification, the mRNA was fragmented into short fragments using divalent cations under elevated temperature (Magnesium RNA Fragmentation Module (NEB, cat.e6150, USA) under 94 °C 5-7 min). Then the cleaved RNA fragments were reverse-transcribed to create the cDNA by SuperScript™ II Reverse Transcriptase (Invitrogen, cat. 1896649, USA), which were next used to synthesize U-labeled second-stranded DNAs with E. coli DNA polymerase I (NEB, cat.m0209, USA), RNase H (NEB, cat.m0297, USA) and dUTP Solution (Thermo Fisher, cat.R0133, USA). An A-base was then added to the blunt ends of each strand, preparing them for ligation to the indexed adapters. Each adapter contained a T-base

overhang for ligating the adapter to the A-tailed fragmented DNA. Dual-index adapters were ligated to the fragments, and size selection was performed with AMPureXP beads. After the heat-labile UDG enzyme (NEB, cat.m0280, USA) treatment of the U-labeled second-stranded DNAs, the ligated products were amplified with PCR by the following conditions: initial denaturation at 95 °C for 3 min; 8 cycles of denaturation at 98 °C for 15 s, annealing at 60 °C for 15 s, and extension at 72 °C for 30 s; and then final extension at 72 °C for 5 min. The average insert size for the final cDNA libraries were 300 ± 50 bp. At last, we performed the 2 × 150 bp paired-end sequencing (PE150) on an Illumina Novaseq™ 6000 (LC-Bio Technology CO., Ltd., Hangzhou, China) following the vendor's recommended protocol. Reads obtained from the sequencing machines includes raw reads containing adapters or low-quality bases which will affect the following assembly and analysis. Thus, to get high quality clean reads, reads were further filtered by Cutadapt (https://cutadapt.readthedocs.io/en/stable/, version:cutadapt-1.9). The parameters were as follows: (1) removing reads containing adapters; (2) removing reads containing polyA and polyG; (3) removing reads containing more than 5% of unknown nucleotides (N); (4) removing low quality reads containing more than 20% of low quality (Q-value ≤ 20) bases. Then sequence quality was verified using FastQC (http://www.bioinformatics.babraham.ac.uk/projects/fastqc/, 0.11.9). including the Q20, Q30 and GC-content of the clean data. After that, a total of G bp of cleaned, paired-end reads were produced. Genes differential expression analysis was performed by DESeq2 software between two different groups (and by edgeR between two samples). The genes with the parameter of false discovery rate (FDR) below 0.05 and absolute fold change ≥ 2 were considered differentially expressed genes. Differentially expressed genes were then subjected to enrichment analysis of KEGG pathways.

Whole exon sequencing

Genomic DNA was extracted using Vazyme FastPure Blood/Cell/Tissue/Bacteria DNAIsolation Mini Kit in accordance with the manufacturer's protocol. The size of genomic DNA fragments was examined by Agilent 4200 TapeStation system (Agilent, Santa Clara, CA, USA). 1 μg of genomic DNA was sheared using enzyme dsDNA Fragmentase for construction of libraries. Hybridization-based target enrichment was conducted with Agilent SureSelect Human All Exon V6. The concentration of the libraries was assessed using Qubit®3.0 Fluorometerand QuantStudio 3 qPCR. The distribution of segments in library was examined by Agilent 4200. Whole human exons were captured using a Agilent SureSelect Human All Exon V6. The DNA sequencing was then performed on the Illumina Novaseq 6000 system. Sequencing was done with 2 × 150 bp paired-end reads, and 850 G per lane were pooled. Raw sequencing reads were preprocessed by fastp v0.12.4 for subsequent analysis. The cleaned reads were aligned to the reference human genome (build hg19) using Sentieon BWA. Sentieon driver was used to sorting reads and remove duplicate reads. Somatic variants (SNVs, InDels and CNVs) were determined using MuTect2 and CNVkit. The whole Exon sequencing and data analysis were conducted by HaploX Technology CO., Ltd., (Jiangxi, China).

In vivo treatment study

BALB/c nude mice (female, 5 weeks) were obtained from Zhejiang Provincial Laboratory Animal Center (Zhejiang, China). Mice were housed under specific-pathogen-free (SPF) conditions with a 12 h/12 h light/dark cycle at 21 °C and 50–55% humidity at the animal facilities of Hangzhou Institute of Medicine (HIM), Chinese Academy of Sciences. The study design and analysis did not account for sex as a variable. No sex-specific data were collected in this study, as investigating sex-based effects was outside the scope of our research focus.

PC9/GR cells (1×10^6 cells per mouse) were subcutaneously inoculated in the back of right forelimbs of nude mice. When the tumor size reached approximately 100 mm³, defined as day 0, the mice were randomly divided into seven groups (five mice per group) and treated with DPBS, gefitinib, gefitinib plus ZAJ4a, gefitinib plus 7D12, gefitinib plus ZAJ4a-7D12, gefitinib plus SL1 or gefitinib plus ZAJ4a-SL1. Gefitinib was administered orally by gavage daily at the concentration of 30 mg/kg. ZAJ4a, 7D12, ZAJ4a-7D12, SL1 and ZAJ4a-SL1 were administered intravenously into the lateral tail veins every 2 days (aptamer was 10 nmol per mouse, 7D12 was 200 ug per mouse). The in vivo study included two parts, EGFR target experiment and Met target experiment. Every part experiment was including five groups. DPBS group, gefitinib group (Gef), gefitinib plus ZAJ4a group (Gef + ZAJ4a), gefitinib plus 7D12 group (Gef + 7D12), gefitinib plus ZAJ4a-7D12 group (Gef + ZAJ4a-7D12) were for EGFR target experiment ($n = 5$ mice for each group). DPBS group, gefitinib group (Gef), gefitinib plus ZAJ4a group (Gef + ZAJ4a), gefitinib plus SL1 group (Gef + SL1), gefitinib plus ZAJ4a-SL1 group (Gef + ZAJ4a-SL1) were for Met target experiment ($n = 5$ mice for each group). Treatments were given as described for 5 times, after which mice were monitored another 1 week for survival experiment. The tumor volume of mice was monitored every 2 days calculated using the following equation: (length × width²)/2. The tumor growth inhibition ratio (%) was calculated by the following equation: [1 – (change of tumor volume in treatment group/change of tumor volume in DPBS group)] × 100. At study termination, mice were sacrificed, and tumor tissues were isolated and weighted. Tumor samples obtained were fixed with 4% paraformaldehyde and embedded in paraffin for H&E analysis and immunohistochemistry assay. Major organs were collected for histopathological examination by H&E staining.

H&E and immunohistochemistry staining

Animal tissues were fixed with 4% paraformaldehyde, then dehydrated in a Sakura Tissue-Tek VIP (Sakura Finetek USA, Torrance, CA) and paraffin embedded with a Leica EG 1160 (Leica Biosystems, Richmond, IL). H&E staining of sections was processed by a full-automatic dyeing machine (DRS-Prisma-P-JCS&Film-JC2, Sakura). Immunohistochemistry staining of sections was performed using BOND RX fully automated strainers (Leica Biosystems) according to standard procedures.

Statistics and reproducibility

Statistical analysis and data plotting were performed using Prism Graph Pad 8.0. Data are presented as the mean ± SD. Generally, an unpaired two-tailed Student's t-test was used to compare two groups, and an ANOVA analysis was used to compare more than two groups as defined in the figure legends.

Representative images of 1a, 1b, 1 h, 3e, 3b, 4b, 4 d, 4 f, 5e, 6b, 6 d, 6e, 6i were from three independent experiments; representative images of 2b and 3 d were from five independent experiments.

No statistical method was used to predetermine sample size. Experimental sample size and replicate numbers (n) are indicated in the figure legends. The experimental groups were randomly assigned. Data acquisition and analysis were performed randomly. No data were excluded from the analysis. No blinding was carried out for data collection and analysis. All experiments were assigned into different groups, and all data was analyzed automatically. Thus, analysis was done objectively and without bias.

Reporting summary

Further information on research design is available in the Nature Portfolio Reporting Summary linked to this article.

Data availability

The data supporting the findings of this study are all available in the manuscript and its supplementary information. Source data are provided with this paper. The whole exome sequencing data generated in this study have been deposited in the NCBI Sequence Read Archive (SRA) database under accession code PRJNA1233638 [http://www.ncbi.

nlm.nih.gov/bioproject/1233638]. Source data are provided with this paper.

References

1. Hunter, T. Signaling–2000 and beyond. *Cell* **100**, 113–127 (2000).
2. Lemmon, M. A. & Schlessinger, J. Cell signaling by receptor tyrosine kinases. *Cell* **141**, 1117–1134 (2010).
3. Du, Z. & Lovly, C. M. Mechanisms of receptor tyrosine kinase activation in cancer. *Mol. Cancer* **17**, 58 (2018).
4. Yamaoka, T., Kusumoto, S., Ando, K., Ohba, M. & Ohmori, T. Receptor tyrosine kinase-targeted cancer therapy. *Int. J. Mol. Sci.* **19**, 3491 (2018).
5. Yang, Z. et al. Comparison of gefitinib, erlotinib and afatinib in non-small cell lung cancer: a meta-analysis. *Int. J. Cancer* **140**, 2805–2819 (2017).
6. Wang, Z. F., Ren, S. X., Li, W. & Gao, G. H. Frequency of the acquired resistant mutation T790M in non-small cell lung cancer patients with active exon 19Del and exon 21 L858R: a systematic review and meta-analysis. *BMC Cancer* **18**, 148 (2018).
7. Montagut, C. et al. Identification of a mutation in the extracellular domain of the epidermal growth factor receptor conferring cetuximab resistance in colorectal cancer. *Nat. Med.* **18**, 221–223 (2012).
8. Zhou, J., Ji, Q. & Li, Q. Resistance to anti-EGFR therapies in metastatic colorectal cancer: underlying mechanisms and reversal strategies. *J. Exp. Clin. Cancer Res.* **40**, 328 (2021).
9. Cohen, P. The origins of protein phosphorylation. *Nat. Cell Biol.* **4**, 127–130 (2002).
10. Leonard, D. et al. Selective PP2A enhancement through biased heterotrimer stabilization. *Cell* **181**, 688–701 (2020).
11. Fernandes, R. A. et al. Immune receptor inhibition through enforced phosphatase recruitment. *Nature* **586**, 779–784 (2020).
12. Yamazoe, S. et al. Heterobifunctional molecules induce dephosphorylation of kinases-a proof of concept study. *J. Med. Chem.* **63**, 2807–2813 (2020).
13. Zhang, Q. et al. Protein phosphatase 5-recruiting chimeras for accelerating apoptosis-signal-regulated kinase 1 dephosphorylation with antiproliferative activity. *J. Am. Chem. Soc.* **145**, 1118–1128 (2023).
14. Zhou, J. & Rossi, J. Aptamers as targeted therapeutics: current potential and challenges. *Nat. Rev. Drug Discov,* **16**, 440 (2017).
15. Du, Y. & Grandis, J. R. Receptor-type protein tyrosine phosphatases in cancer. *Chin. J. Cancer* **34**, 61–69 (2015).
16. Gan, T. et al. Inhibition of protein tyrosine phosphatase receptor type F suppresses Wnt signaling in colorectal cancer. *Oncogene* **39**, 6789–6801 (2020).
17. Lv, J. et al. Generation of an aptamer targeting receptor-type tyrosine-protein phosphatase F. *Anal. Chem.* **95**, 1228–1233 (2023).
18. Hong, H. et al. Chemoenzymatic synthesis of a rhamnose-functionalized bispecific nanobody as a bispecific antibody mimic for cancer immunotherapy. *Angew. Chem. Int. Ed* **61**, e202208773 (2022).
19. Wang, L. et al. Bispecific aptamer induced artificial protein-pairing: a strategy for selective inhibition of receptor function. *J. Am. Chem. Soc.* **141**, 12673–12681 (2019).
20. Lin, Z. et al. Multi-scale photocatalytic proximity labeling reveals cell surface neighbors on and between cells. *bioRxiv* **29**, 2023.10.28.564055 (2023).
21. Yao, Z. et al. A global analysis of the receptor tyrosine kinase-protein phosphatase interactome. *Mol. Cell* **65**, 347–360 (2017).
22. Zhang, F. et al. Quantification of epidermal growth factor receptor expression level and binding kinetics on cell surfaces by surface plasmon resonance imaging. *Anal. Chem.* **87**, 9960–9965 (2015).
23. Liang, H. et al. Nongenetic approach for imaging protein dimerization by aptamer recognition and proximity-induced DNA assembly. *J. Am. Chem. Soc.* **140**, 4186–4190 (2018).
24. Ren, Y. et al. EGF/EGFR Promotes salivary adenoid cystic carcinoma cell malignant neural invasion via activation of PI3K/AKT and MEK/ERK signaling. *Curr. Cancer Drug Targets* **22**, 603–616 (2022).
25. Serrano-Gomez, S. J., Maziveyi, M. & Alahari, S. K. Regulation of epithelial-mesenchymal transition through epigenetic and post-translational modifications. *Mol. Cancer* **15**, 18 (2016).
26. Zhao, M., Liu, Y., Zheng, C. & Qu, H. dbEMT 2.0: An updated database for epithelial-mesenchymal transition genes with experimentally verified information and precalculated regulation information for cancer metastasis. *J. Genet Genomics* **46**, 595–597 (2019).
27. Li, Y. et al. Nanoengineered gallium ion incorporated formulation for safe and efficient reversal of parp inhibition and platinum resistance in ovarian cancer. *Research* **6**, 1–16 (2023).
28. Shah, R. & Lester, J. F. Tyrosine kinase inhibitors for the treatment of EGFR mutation-positive non-small-cell lung cancer: a clash of the generations. *Clin. Lung Cancer* **21**, 216–228 (2020).
29. Yun, C. H. et al. The T790M mutation in EGFR kinase causes drug resistance by increasing the affinity for ATP. *Proc. Natl Acad. Sci. USA* **105**, 2070–2075 (2008).
30. Chou, T. C. Theoretical basis, experimental design, and computerized simulation of synergism and antagonism in drug combination studies. *Pharmacol. Rev.* **58**, 621–681 (2006).
31. Hu, S. et al. The synergistic effect of resveratrol in combination with cisplatin on apoptosis via modulating autophagy in A549 cells. *Acta Biochim. Biophys. Sin. (Shanghai)* **48**, 528–535 (2016).
32. Linardou, H. et al. Assessment of somatic k-RAS mutations as a mechanism associated with resistance to EGFR-targeted agents: a systematic review and meta-analysis of studies in advanced non-small-cell lung cancer and metastatic colorectal cancer. *Lancet Oncol.* **9**, 962–972 (2008).
33. Yuan, J., Dong, X., Yap, J. & Hu, J. The MAPK and AMPK signalings: interplay and implication in targeted cancer therapy. *J. Hematol. Oncol.* **13**, 113 (2020).
34. Yi, M. et al. Targeting cytokine and chemokine signaling pathways for cancer therapy. *Signal Transduct. Tar.* **9**, 176 (2024).
35. Bong, A. H. L. & Monteith, G. R. Calcium signaling and the therapeutic targeting of cancer cells. *Biochim. Biophys. Acta Mol. Cell Res.* **1865**, 1786–1794 (2018).
36. Evan, G. I. & Vousden, K. H. Proliferation, cell cycle and apoptosis in cancer. *Nature* **411**, 342–348 (2001).
37. Engelman, J. A. et al. MET amplification leads to gefitinib resistance in lung cancer by activating ERBB3 signaling. *Science* **316**, 1039–1043 (2007).
38. Wang, Q., Yang, S., Wang, K. & Sun, S. Y. MET inhibitors for targeted therapy of EGFR TKI-resistant lung cancer. *J. Hematol. Oncol.* **12**, 63 (2019).
39. Martinelli, E. et al. Implementing anti-epidermal growth factor receptor (EGFR) therapy in metastatic colorectal cancer: challenges and future perspectives. *Ann. Oncol.* **31**, 30–40 (2020).
40. Liu, Q. et al. EGFR-TKIs resistance via EGFR-independent signaling pathways. *Mol. Cancer* **17**, 53 (2018).
41. Ambrosini, G. et al. Inhibition of NF-kappaB-dependent signaling enhances sensitivity and overcomes resistance to BET inhibition in uveal melanoma. *Cancer Res.* **79**, 2415–2425 (2019).
42. Fan, Y. et al. Rack1 mediates tyrosine phosphorylation of Anxa2 by Src and promotes invasion and metastasis in drug-resistant breast cancer cells. *Breast Cancer Res.* **21**, 66 (2019).
43. Jeddi, I. & Saiz, L. Three-dimensional modeling of single stranded DNA hairpins for aptamer-based biosensors. *Sci. Rep.* **7**, 1178 (2017).
44. de Vries, S. J., van Dijk, M. & Bonvin, A. M. The HADDOCK web server for data-driven biomolecular docking. *Nat. Protoc.* **5**, 883–897 (2010).
45. Van Der Spoel, D. et al. GROMACS: fast, flexible, and free. *J. Comput. Chem.* **26**, 1701–1718 (2005).

46. Yu, Y. L. et al. Semi-automated optimization of the CHARMM36 lipid force field to include explicit treatment of long-range dispersion. *J. Chem. Theory Comput.* **17**, 1562–1580 (2021).

47. Darden, T., York, D. & Pedersen, L. Particle mesh Ewald - an N.Log(N) method for Ewald sums in large systems. *J. Chem. Phys.* **98**, 10089–10092 (1993).

48. Luzar, A. & Chandler, D. Structure and hydrogen bond dynamics of water–dimethyl sulfoxide mixtures by computer simulations. *J. Chem. Phys.* **98**, 8160–8173 (1993).

49. de Jong, D. H. et al. Improved parameters for the martini coarse-grained protein force field. *J. Chem. Theory Comput.* **9**, 687–697 (2013).

50. Periole, X., Cavalli, M., Marrink, S. J. & Ceruso, M. A. Combining an elastic network with a coarse-grained molecular force field: structure, dynamics, and intermolecular recognition. *J. Chem. Theory Comput.* **5**, 2531–2543 (2009).

51. Koldso, H., Shorthouse, D., Helie, J. & Sansom, M. S. Lipid clustering correlates with membrane curvature as revealed by molecular simulations of complex lipid bilayers. *PLoS Comput. Biol.* **10**, e1003911 (2014).

52. Parrinello, M. & Rahman, A. Polymorphic transitions in single crystals: a new molecular dynamics method. *J. Appl. Phys.* **52**, 7182–7190 (1981).

53. Tironi, I. G., Sperb, R., Smith, P. E. & van Gunsteren, W. F. A generalized reaction field method for molecular dynamics simulations. *J. Chem. Phys.* **102**, 5451–5459 (1995).

54. Hess B., Bekker H., Berendsen H. J. C., Fraaije J. G. E. M. LINCS: A linear constraint solver for molecular simulations. **18**, 1463–1472 (1997).

Acknowledgements

Author contributions

Zhilan Zhou and Juan Li conceptualized the project and designed the study. Zhilan Zhou conducted the all experiments, analyzed the data and drafted the manuscript. Yichang Liu conducted structure modeling and molecular dynamic simulations. Ya Wang, Tingting Chen and Hang Jiang helped with in vivo experiments. Ting Fu and Yingdi Zhu helped with data analysis and language polishing. Juan Li provided financial support for the study, supervised the project and revised the manuscript.

Competing interests

The authors declare no competing interests.

Additional information

Supplementary information The online version contains supplementary material available at https://doi.org/10.1038/s41467-025-59098-2.

Correspondence and requests for materials should be addressed to Juan Li.

Peer review information *Nature Communications* thanks Tyler Reddy, Vittorio de Franciscis, and the other, anonymous, reviewer(s) for their contribution to the peer review of this work. A peer review file is available.

Reprints and permissions information is available at http://www.nature.com/reprints

Publisher's note Springer Nature remains neutral with regard to jurisdictional claims in published maps and institutional affiliations.